FACULTY OF ASTROPHYSICS, GEOPHYSICS
AND OCEANOGRAPHY

Modelling gravitationally lensed quasars from hydrodynamical simulations: Successes and limitations

Guillaume ALLEMAND

Board of reviewers:
Pr. Pierre Magain
Dr. Damien Hutsemékers
Dr. Christian Barbier
Dr. Ludovic Delchambre

Supervisor:
Dr. Dominique Sluse

Thesis submitted in partial fulfillment of the requirements for the degree of Master in space sciences

Academic Year 2019-2020

Acknowledgements

I would like to thank my supervisor, Dominique Sluse for his support and all the advice he gave me during this year, especially during the last days (even hours) preceding the deposit of my master thesis. I want also to thank the members of the board of reviewers for accepting to be part of it and for the time they will spend to read my Master thesis. Moreover, I want to express my gratitude to Lyne Van de Vyvere who accepted to answer to my questions about the topics addressed in this thesis.

I thank my family for supporting me during these tough years, as well as my friends Louis, Boris, Valentin, Eliott, Nikita, Dima, Mathilde and Pierre.

Contents

Chapter 1

Purpose and organisation

1.1 Purpose

Gravitational lensing is a phenomenon occurring when light emitted by distant galaxies passes close to massive objects in the universe. This light can be distorted and bended under the gravitational influence of these objects. The study of gravitationally lensed quasars is very useful in cosmology and astrophysics because it allows one to infer the value of the Hubble constant H_0, to reveal substructures along the line-of-sight of distant galaxies and to analyze the mass distribution of lensing galaxies, i.e. determine the shape and the slope of baryons and dark matter distributions in the inner regions of galaxies [22].

Gravitational lensing offers the opportunity to measure H_0 with a precision becoming very high, reaching nowadays an uncertainty $< 2.5\%$ from an ensemble of 7 systems [25]. However, it might still remain bias and uncertainties in the measurement of H_0. In order to evaluate the importance of these uncertainties, instead of trying to deduce H_0 from a real gravitational lens system, it is interesting to simulate and study a lensing system using a lens galaxy created by hydrodynamical simulations.
Tagore et al. [23], as well as Xu et al. [27] have presented such a working method, Tagore et al. obtaining very good results to reduce the bias on the measurements of H_0. In their studies, they used a power-law model to characterize the mass density profile of the lens because real cases are generally modeled with power-law models. Indeed, as found by Koopmans et al. [12] and Gavazzi et al. [5], the density profile in the inner region of galaxies is well approximated by a power-law model [27]. Nonetheless, the issue is that the power-law model is just an approximation of the radial profile of a galaxy and it is not demonstrated that this approximation does not introduce bias on H_0. Therefore, the choice of the lens mass model in the modelling of hydrodynamically simulated galaxies appears to be very fundamental.

The purpose of this master thesis is to test the ability of an analytical mass model to reproduce the properties of a non-analytical (or realistic) lens galaxy generated by hydrodynamical simulations.

1.2 Organisation

This thesis is divided into several chapters in order to approach the purpose mentioned above in a coherent way.

Firstly, in Chapter 2, the gravitational lens theory is introduced, summarizing and emphasizing the required notions to understand the concepts subsequently discussed.
Secondly, in Chapter 3, the principles of modelling are introduced, explaining what is lens modelling and how the software that allows one to model lenses works.
Thirdly, in Chapter 4, a first lens modelling is presented, considering a lens galaxy generated with an analytical lens model in order to see if the properties of the lens are well retrieved in such a simple case.

Then, in Chapter 5, the purpose of this master thesis is addressed, a realistic lens galaxy created by hydrodynamical simulations is modeled for different lensing configurations, the results are analyzed and discussed in an attempt to see if the inferred properties of the lens galaxy seem to be plausible.

Finally, in the conclusion, the results obtained in Chapters 4 and 5 are compared and various approaches to improve these results are mentioned.

Chapter 2

Gravitational lens theory

According to General Relativity, light and electromagnetic waves in general propagate along null geodesics of the space-time metric. The description of the behaviour of light rays by General Relativity equations is rather complicated and is only mandatory for light rays passing near strong gravitational fields such as those of neutron stars or black holes. An easier description of the behaviour of light rays can be done in most astrophysical situations which are in a regime of small deflection angles and weak gravitational fields (for example gravitational lensing by galaxies and clusters of galaxies). This is the geometric description of the gravitational lens theory. In this chapter, the basics of the geometric gravitational lens theory will be summarized, the essential lens equation will be introduced as well as its applications. This chapter follows the structure of the Part 1 of the book *Gravitational lensing: strong, weak and micro* [21].

2.1 The deflection angle

The deflection angle of a light ray, passing in a gravitational field induced by a spherically symmetric mass M at distance ξ from its center, is

$$\hat{\alpha} = \frac{4GM}{c^2\xi}\,, \tag{2.1}$$

as predicted by General relativity. G is the constant of gravitation and c is the velocity of light. However, this equation is valid only if the impact parameter ξ is larger than the Schwarzschild radius of the mass, namely $\xi \gg R_s \equiv 2GMc^{-2}$. Under this condition, the deflection angle $\hat{\alpha}$ is very small ($\ll 1$).
Nonetheless, as mentioned above, if the gravitational field is weak, approximations can be done and the equations of General Relativity can be linearized. In this scenario,

the mass can be divided into an ensemble of mass elements and the deflection angle can be considered as a vectorial sum of deflections produced by each mass component. Mathematically, this two-dimensional vector can be written as :

$$\begin{aligned}\hat{\boldsymbol{\alpha}}(\boldsymbol{\xi}) &= \frac{4G}{c^2}\sum \mathrm{d}m\left(\xi_1', \xi_2', r_3'\right)\frac{\boldsymbol{\xi}-\boldsymbol{\xi}'}{\left|\boldsymbol{\xi}-\boldsymbol{\xi}'\right|^2} \\ &= \frac{4G}{c^2}\int \mathrm{d}^2\xi' \int \mathrm{d}r_3'\rho\left(\xi_1', \xi_2', r_3'\right)\frac{\boldsymbol{\xi}-\boldsymbol{\xi}'}{\left|\boldsymbol{\xi}-\boldsymbol{\xi}'\right|^2}\,.\end{aligned} \tag{2.2}$$

In this equation, one considers a three-dimensional mass distribution of volume density $\rho(\boldsymbol{r})$ which can be divided into elements of mass $\mathrm{d}m = \rho(\boldsymbol{r})\mathrm{d}V$ and volume $\mathrm{d}V$. The system of coordinates describing the trajectory of the light ray is chosen such as its spatial trajectory is written $(\xi_1(\lambda), \xi_2(\lambda), r_3(\lambda))$, with λ which parametrizes the curved trajectory of the light ray and when it is far from the deflector, it propagates along r_3.

Since the mass distribution is usually small in terms of size compared to the distances travelled by the light rays and if the deflection angle is small, a useful approximation called *geometrically-thin lens* can be made. This approximation allows the light rays to be considered as straight lines and the volume density of the lens can be projected onto a plane perpendicular to the light ray, as shown in Figure 2.1. In this context, the impact vector $\boldsymbol{\xi} = (\xi_1, \xi_2)$ (a two-dimensional vector) is independent of the affine parameter λ which parametrizes the trajectory.

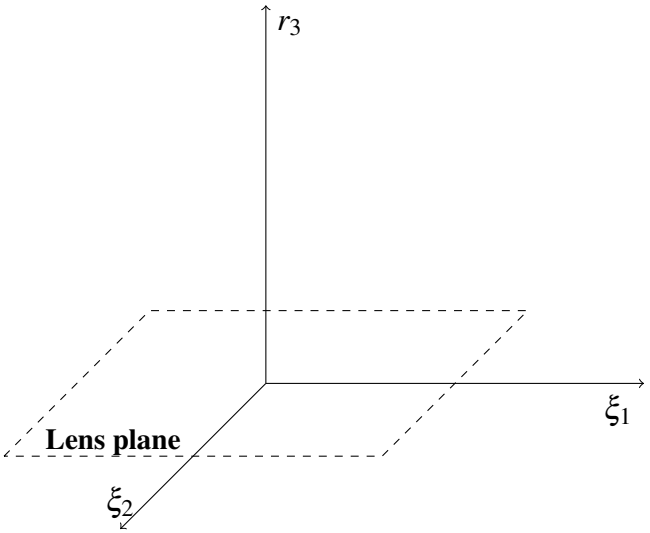

Figure 2.1: Representation of the coordinates system with respect to the lens plane, the axis r_3 is oriented along the optical axis.

Moreover, the coordinates of the mass element dm are written $\boldsymbol{r}' = \left(\xi_1', \xi_2', r_3'\right)$ and the impact vector of the light ray relative to the mass element is thus $\boldsymbol{\xi} - \boldsymbol{\xi}'$. Since this impact vector is independent of r_3' and by introducing the *surface mass density*

$$\Sigma(\boldsymbol{\xi}) \equiv \int \mathrm{d}r_3 \rho\left(\xi_1, \xi_2, r_3\right) \ , \tag{2.3}$$

which is the mass density projected on the plane perpendicular to the light ray. One can rewrite the expression of the deflection angle produced by an arbitrary density distribution such that :

$$\hat{\boldsymbol{\alpha}}(\boldsymbol{\xi}) = \frac{4G}{c^2} \int \mathrm{d}^2\xi' \Sigma\left(\boldsymbol{\xi}'\right) \frac{\boldsymbol{\xi} - \boldsymbol{\xi}'}{\left|\boldsymbol{\xi} - \boldsymbol{\xi}'\right|^2} \ . \tag{2.4}$$

2.2 The lens equation

The standard situation introduced in the previous section is represented in Figure 2.2. The light ray can be approximated as a straight line because large distances, compared to the dimensions of the lens, are considered and because a unique deflector is taken into account. Indeed, more sophisticated models can consider other deflecting masses along the line-of-sight and in that case, the representation is much more complicated than the one sketched here.

A light ray, emitted by a source at distance D_s from the observer, is deflected by a lens at distance D_d with a deflection angle $\hat{\boldsymbol{\alpha}}$ expressed by the relation (2.4). Note that the distances considered here are angular diameter distances, but can also be written in terms of redshifts. The expression of the angular diameter distances depend on the cosmographic parameters, hence also on the geometry of the universe and $D_s \neq D_d + D_{ds}$ [7].

Furthermore, one can define the source plane and the lens plane which are perpendicular to the optical axis (in bold dotted lines). Finally, $\boldsymbol{\eta}$ corresponds to the two-dimensional vector expressing the position of the source with respect to the intersection between the source plane and the optical axis.

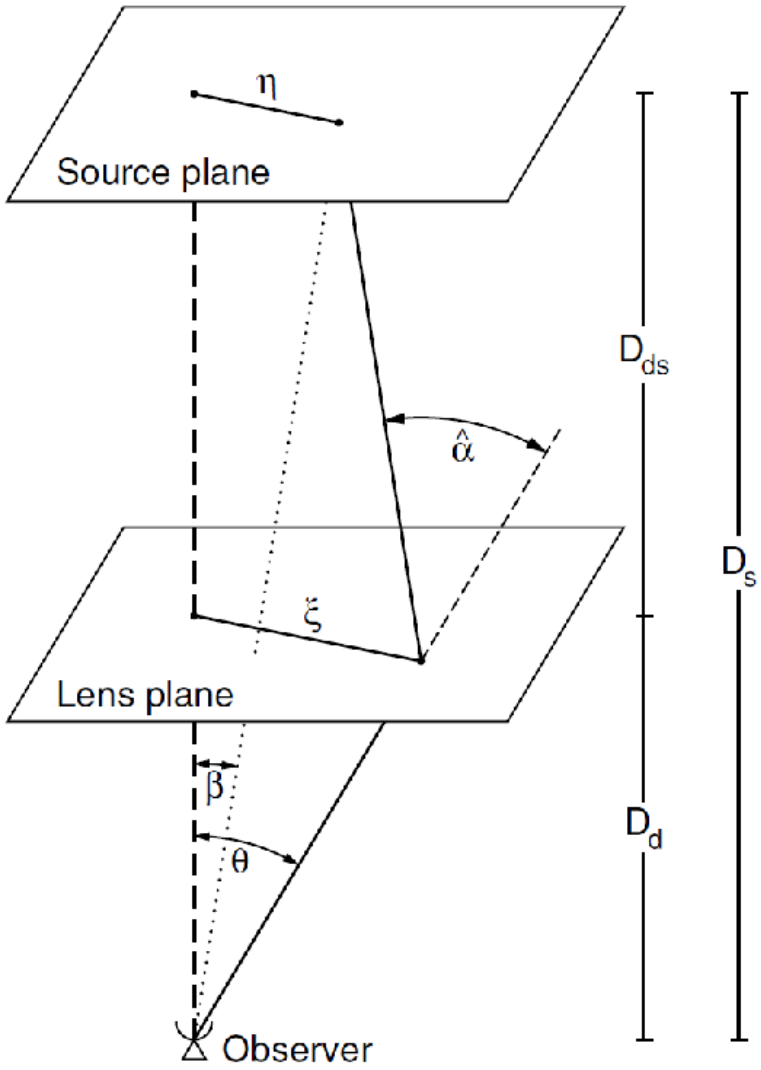

Figure 2.2: Representation of a classic gravitational lens system [21].

From Figure 2.2 and considering that the angles are small ($\sin\hat{\alpha} \approx \hat{\alpha} \approx \tan\hat{\alpha}$), one can establish the geometric condition :

$$\boldsymbol{\eta} = \frac{D_\mathrm{s}}{D_\mathrm{d}}\boldsymbol{\xi} - D_\mathrm{ds}\hat{\boldsymbol{\alpha}}(\boldsymbol{\xi}) \,. \tag{2.5}$$

By introducing the angular coordinates

$$\boldsymbol{\eta} = D_\mathrm{S}\boldsymbol{\beta} \text{ and } \boldsymbol{\xi} = D_\mathrm{d}\boldsymbol{\theta} \,, \tag{2.6}$$

(2.5) becomes

$$\boldsymbol{\beta} = \boldsymbol{\theta} - \frac{D_{\mathrm{ds}}}{D_{\mathrm{s}}}\hat{\boldsymbol{\alpha}}\left(D_{\mathrm{d}}\boldsymbol{\theta}\right) \equiv \boldsymbol{\theta} - \boldsymbol{\alpha}(\boldsymbol{\theta})\,, \tag{2.7}$$

where $\boldsymbol{\alpha}(\boldsymbol{\theta}) = \frac{D_{\mathrm{ds}}}{D_{\mathrm{s}}}\hat{\boldsymbol{\alpha}}\left(D_{\mathrm{d}}\boldsymbol{\theta}\right)$ is the *scaled deflection angle*. The equation (2.7) is the lens equation and expresses the fact that a source at an angular position $\boldsymbol{\beta}$ is seen by the observer at the angular position(s) $\boldsymbol{\theta}$ which is (are) solution(s) of the equation. The conditions under which multiple images are created will be introduced later on.
The lens equation (2.7) defines, in fact, a mapping from the lens plane to the source plane $\boldsymbol{\theta} \to \boldsymbol{\beta}$. This mapping is easily calculated if the expression of the surface mass density $\Sigma(\boldsymbol{\xi})$ is known, i.e. if the (scaled) deflection angle can be calculated. The main issue in gravitational lensing, as we will see in the next chapter, is to make the inversion of the lens equation (2.7). In other words, it consists in deducing all the images positions $\boldsymbol{\theta}$ on the basis of the source position $\boldsymbol{\beta}$.

Furthermore, one can introduce now a very important quantity, the *Einstein radius* θ_E. Using (2.1) and (2.6) and replacing it into (2.7), if a point source is situated at $\boldsymbol{\beta} = 0$, perfectly behind a lens with spherical symmetry, then the solution of the lens equation would be :

$$\theta_E = \sqrt{\frac{4GM}{c^2}\frac{D_{ds}}{D_d D_s}}\,, \tag{2.8}$$

with M, the lens mass inside the Einstein radius.
This specific arrangement results in a source imaged into a ring of radius θ_E, a so-called *Einstein ring*. However, one does not obtain such a ring when an elliptical lens is considered. Nonetheless, the Einstein radius can be calculated for any mass distribution and it turns out to be an important quantity in gravitational lensing because the typical opposed images separation can be approximated such that $\Delta\theta \approx 2\theta_E$ [13, 21, 24].

Moreover, the scaled deflection angle can be expressed in terms of the *dimensionless surface mass density*, also called *convergence*, $\kappa(\boldsymbol{\theta})$:

$$\boldsymbol{\alpha}(\boldsymbol{\theta}) = \frac{1}{\pi}\int_{\mathbb{R}^2} \mathrm{d}^2\theta' \kappa\left(\boldsymbol{\theta}'\right)\frac{\boldsymbol{\theta} - \boldsymbol{\theta}'}{\left|\boldsymbol{\theta} - \boldsymbol{\theta}'\right|^2} \tag{2.9}$$

$$\text{and } \kappa(\boldsymbol{\theta}) = \frac{\Sigma\left(D_{\mathrm{d}}\boldsymbol{\theta}\right)}{\Sigma_{\mathrm{cr}}} \quad \text{with} \quad \Sigma_{\mathrm{cr}} = \frac{c^2}{4\pi G}\frac{D_{\mathrm{s}}}{D_{\mathrm{d}}D_{\mathrm{ds}}}\,, \tag{2.10}$$

where Σ_{cr} is the *critical surface mass density* which will be useful in the discussion of the conditions to obtain multiple images that will be addressed later.

Furthermore, using the identity $\nabla \ln|\boldsymbol{\theta}| = \boldsymbol{\theta}/|\boldsymbol{\theta}|^2$ which is valid for any two-dimensional vector $\boldsymbol{\theta}$, one can define the *deflection potential*

$$\psi(\boldsymbol{\theta}) = \frac{1}{\pi}\int_{\mathbb{R}^2} \mathrm{d}^2\theta' \kappa\left(\boldsymbol{\theta}'\right) \ln\left|\boldsymbol{\theta} - \boldsymbol{\theta}'\right| . \tag{2.11}$$

The scaled deflection angle can thus be written as :

$$\boldsymbol{\alpha} = \nabla\psi \tag{2.12}$$

and the mapping $\boldsymbol{\theta} \to \boldsymbol{\beta}$ becomes a gradient mapping.
Then, one can derive another useful relation for the future, using the identity $\nabla^2 \ln|\boldsymbol{\theta}| = 2\pi\delta_{\mathrm{D}}(\boldsymbol{\theta})$ with δ_{D} the Dirac delta in two dimensions. From (2.11), one gets the *Poisson equation* in two dimensions :

$$\nabla^2\psi = 2\kappa . \tag{2.13}$$

In addition, one introduces a scalar function that will turn out to be very important, the *Fermat potential* :

$$\tau(\boldsymbol{\theta};\boldsymbol{\beta}) = \frac{1}{2}(\boldsymbol{\theta} - \boldsymbol{\beta})^2 - \psi(\boldsymbol{\theta}) , \tag{2.14}$$

which is a function of $\boldsymbol{\theta}$ with $\boldsymbol{\beta}$ as a parameter. Moreover, $\tau(\boldsymbol{\theta};\boldsymbol{\beta})$ is actually, up to an affine transformation, the travel time of a lensed light ray from the source to the observer [20]. The time delay between an image denoted (1) and an image denoted (2) is in fact expressed as :

$$\Delta t = \frac{D_{\mathrm{D}}^{\mathrm{ang}} D_{\mathrm{s}}^{\mathrm{ang}}}{c D_{\mathrm{ds}}^{\mathrm{ang}}} (1 + z_{\mathrm{d}}) \left[\tau\left(\boldsymbol{\theta}^{(1)};\boldsymbol{\beta}\right) - \tau\left(\boldsymbol{\theta}^{(2)};\boldsymbol{\beta}\right)\right] , \tag{2.15}$$

where the distances are expressed in terms of angular diameter distances and z_{d} is the redshift of the deflector. Hence, the time delays between the different images are due to the differences in terms of optical paths and also due to the differences in terms of the deflection potential $\psi(\boldsymbol{\theta})$ which produces a kind of "gravitational slow-down" [13]. Moreover, the Hubble constant H_0 can be inferred from the relation (2.15) and the latter is the key to make cosmography from time delays [11, 15]. A relevant explanation of the time delay is given by considering the propagation of a wave front, the images get formed where the wave front is stationary [19]. This is the Fermat principle expressed as :

$$\nabla\tau(\boldsymbol{\theta};\boldsymbol{\beta}) = 0 , \tag{2.16}$$

which is equivalent to the lens equation (2.7). In fact, the latter relation is really important because it states that physical light rays are those for which the light travel time is stationary. Thus, all the observed images satisfy to the lens equation and the relation (2.16) and these images have a time delay that is constant.

2.3 Distortion and magnification

This section aims to introduce the distortion and the magnification as well as their causes. However, going into too much details would be complicated and not very useful. Hence, only relevant information for this thesis will be outlined and summarized.
In the previous section, the lens equation and its solutions $\boldsymbol{\theta}$, the angular positions of the images of a source at $\boldsymbol{\beta}$, were introduced. Nonetheless, the shapes of the images are not the same as the shape of the source simply because the light rays are deflected differentially. If there is no emission or absorption of photons in the considered gravitational lensing, the surface brightness or the specific intensity of the source must be conserved. Indeed, let $I^{(\mathrm{s})}(\boldsymbol{\beta})$ be the surface brightness distribution in the source plane, the observed surface brightness distribution in the lens plane will be

$$I(\boldsymbol{\theta}) = I^{(\mathrm{s})}[\boldsymbol{\beta}(\boldsymbol{\theta})] \, . \tag{2.17}$$

Provided that the extended source is much smaller than the angular scale on which the lens properties change, the lens mapping can be linearized locally. The distortion of the images is given by the Jacobian matrix between the source and the image :

$$\mathcal{A}(\boldsymbol{\theta}) = \frac{\partial \boldsymbol{\beta}}{\partial \boldsymbol{\theta}} = \left(\delta_{ij} - \frac{\partial^2 \psi(\boldsymbol{\theta})}{\partial \theta_i \partial \theta_j} \right) = \begin{pmatrix} 1-\kappa-\gamma_1 & -\gamma_2 \\ -\gamma_2 & 1-\kappa+\gamma_1 \end{pmatrix} , \tag{2.18}$$

where the component of the shear γ have been introduced such that : $\gamma \equiv \gamma_1 + \mathrm{i}\gamma_2 = |\gamma| \mathrm{e}^{2\mathrm{i}\varphi}$, with

$$\gamma_1 = \frac{1}{2}(\psi_{11} - \psi_{22}), \quad \gamma_2 = \psi_{12} \, . \tag{2.19}$$

Note that κ (the convergence) is associated to the deflection potential ψ through the Poisson equation (2.13).
Therefore, from the relation (2.17) and using the locally linearized lens equation, let $\boldsymbol{\theta}_0$ be a point within an image corresponding to the point $\boldsymbol{\beta}_0 = \boldsymbol{\beta}(\boldsymbol{\theta}_0)$ in the source, one has

$$I(\boldsymbol{\theta}) = I^{(\mathrm{s})} \left[\boldsymbol{\beta}_0 + \mathcal{A}(\boldsymbol{\theta}_0) \cdot (\boldsymbol{\theta} - \boldsymbol{\theta}_0) \right] \, . \tag{2.20}$$

The terms in brackets are in fact a first order Taylor development of $\boldsymbol{\beta}(\boldsymbol{\theta})$, where we used (2.18). One can see from this equation that the images of a source with circular isophotes are ellipses.
Furthermore, the magnification tensor is given by the inverse of the Jacobian matrix :

$$M(\boldsymbol{\theta}) = \mathcal{A}^{-1} \, . \tag{2.21}$$

This tensor is very useful because it allows one to make the local mapping from the source to the image plane and it allows also to derive the *magnification* μ of the source,

which is the ratio between the fluxes observed from the image and from the source :

$$\mu = \det M = \frac{1}{\det \mathcal{A}} = \frac{1}{(1-\kappa)^2 - |\gamma|^2} \, . \tag{2.22}$$

Thus, from all these considerations, one understands how and why the images are distorted in shape and size. The shape distortion is due to the shear γ, which in fact characterizes the tidal gravitational field. On the other hand, the magnification is due to the local matter density κ and also to the shear.
Moreover, it is important for future considerations, notably for the section relative to the critical curves and caustics, to notice that the magnification (2.22) can be positive or negative and its sign is called the *parity* of the image, we will come back to that later on.

Finally, one should notice that the observed flux of an image is fixed by the absolute value of μ (absolute value because, as we just said, the magnification, as defined in (2.22), can be negative), but the magnification is not an observable since the luminosity of the source is not known a priori. Nevertheless, the knowledge of the flux ratios with respect to a reference image allows one to measure the magnification ratios with respect to this reference image. Note also that gravitational lensing is achromatic. Indeed, the deflection of the photons does not depend on their frequency, but if the source is extended and unresolved, one can see some color terms on the images. It is due to the fact that the surface brightness $I^{(s)}(\boldsymbol{\beta})$ is not the same at all frequencies, thus, if the magnification varies on scales comparable to the source size, μ can depend on the frequency in these specific conditions. However, in the modelling presented later in this thesis, the source is not resolved and is considered as a point source. Hence, the magnification appears as an "amplification" of the source [19].

2.4 Critical curves and caustics

The *critical curves* are curves defined by $\det\mathcal{A}(\boldsymbol{\theta}) = 0$, standing in the lens plane and they are smooth and closed. Moreover, simply by doing a mapping with the lens equation of these critical curves to the source plane, one can obtain the so-called *caustics*. The caustics are thus in the source plane but, in opposition to the critical curves, they can be not smooth at all in some regions called *cusps*. When the caustic is smooth, it is called *fold caustic*. A representation of these new concepts is done on the Figure 2.3. The critical curves and caustics are really important because they allow to do a qualitative mapping and to know the number of images that will be created, as well as their location, as sketched on the Figures 2.4 and 2.5.

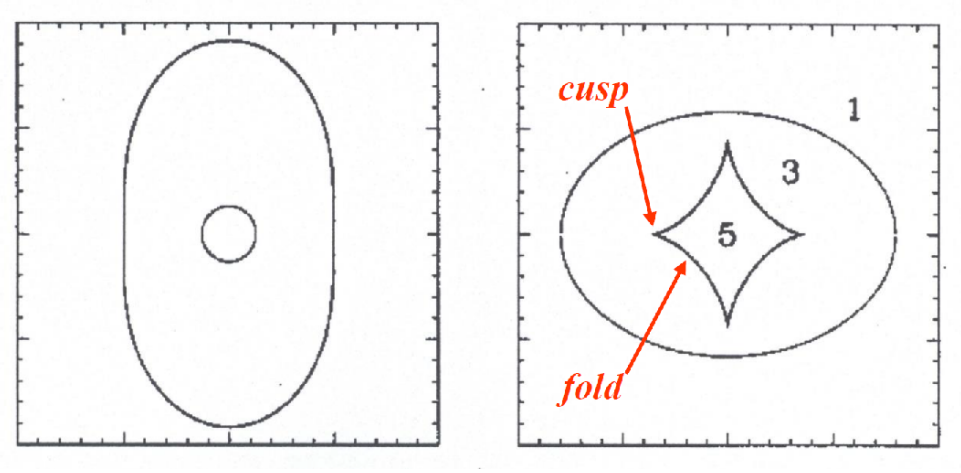

Figure 2.3: Critical curves (left) and caustics (right) for an elliptical lens [13]. The critical curves and the caustics are represented, showing what a cusp and a fold caustic look like, as well as the number of the images according to the source position with respect to the different caustics. The number of images changes by 2 when the source crosses a caustic. In the case of three or five images, one of them is highly attenuated and is located near the center of the lens, leading to the fact that one usually observes only two or four images. Nonetheless, note that only the non-symmetric lenses can generate more than two images (plus the faint image near the center of the lens).

It is however interesting to emphasize some properties of these curves.
Firstly, on a critical curve, $\det\mathcal{A} = 0$ and thus the magnification $\mu = \frac{1}{\det\mathcal{A}}$ diverges. Nonetheless, an infinite magnification is obviously unphysical. To solve this issue, one has to understand that all sources have a finite extent that maintains their observed

magnification finite and even though one considers a point mass source, its magnification would be different from zero because, in this case, the geometrical optics approximation can no longer stand and the wave optics must be used. Hence, the observed magnification is always finite, but one observes a very high magnification of the images near the critical curve in the lens plane when a source is located close to the corresponding caustic in the source plane.
Secondly, the number of images produced in a gravitational lensing system depends on the position of the source compared to the caustic. Indeed, one can see on Figure 2.3 that a source located far away from the center of the lens in terms of angular distance will produce only one image. On the contrary, the source can have multiple images if the impact vector is small. Be careful however with this because it is not strictly speaking a condition for multiple imaging, we will come back to this in a moment. Moreover, one might wonder the conditions for the number of images to change. The lens mapping described by (2.7) can be locally inverted if $\det \mathcal{A} \neq 0$. Thus, since the caustics are mapped in the source plane following the critical curves in the lens plane, the number of images does not change except if the source crosses a caustic. In that case, a pair of images near the corresponding critical curve is created or destroyed depending on the direction of crossing, as shown on Figures 2.4 and 2.5. The side of the caustic where the number of images is bigger than the other is called the "inner side". In fact, a source located near a caustic can have two highly magnified images (in addition to the other potential images) on either side of the corresponding critical curve. Since these images are not on the same side of the critical curve, their magnification μ are equal and opposite in sign (opposite parities) and they merge with another image when the source crosses the caustic from the inner side to the other side. A pair of images is thus destroyed. One might add that a source close to and inside a cusp has three highly magnified images near the corresponding critical curve, while a source close to, but outside a cusp, has only one highly magnified image again near the corresponding critical curve.

Beside all these considerations, the conditions for multiple imaging remain to be addressed. A sufficient condition is that the surface mass density of the lens $\sum$ be greater than the critical surface mass density $\sum_{cr}$ such as $\sum > \sum_{cr}$. In other words, from (2.10), it means that the convergence must be greater than 1, i.e. $\kappa > 1$. The lenses satisfying this condition are called "strong lenses" and hence, it explains why the gravitational lensing resulting in multiple images is called "strong lensing".

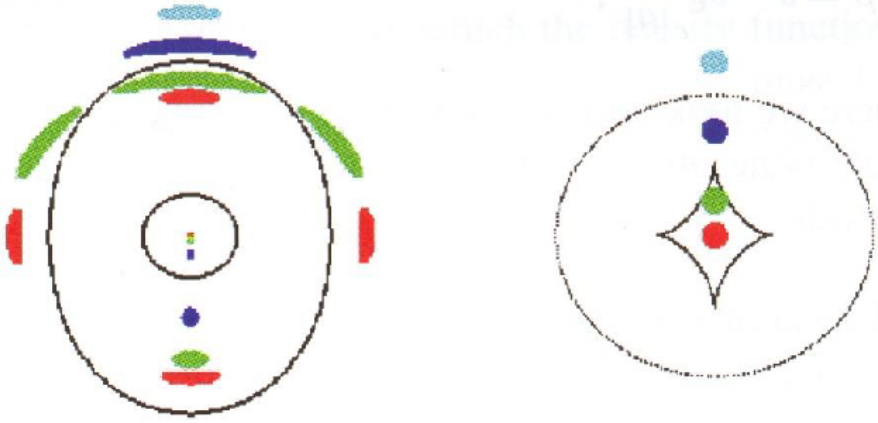

Figure 2.4: Images positions for an elliptical lens in a cusp configuration [13]. The images and the critical curves (in the lens plane) are sketched on the left panel, while the source and the caustics (in the source plane) are illustrated on the right panel. The positions of the images for a source crossing a cusp are represented with different colors in order to see how the images evolve with respect to the source position. The source is considered spherical with a finite extent and, when the source crosses a caustic from the "inner side" to the "outer side", this leads to the merging of three images into one. The central highly attenuated images are sketched as tiny points near the center of the lens galaxy.

In addition, one can also see on Figures 2.4 and 2.5 that, when the source is located near a caustic, there is an emergence of arcs or arclets, which is possible only for extended sources. Finally, note that the figures here are only simple examples of gravitational lensing. Of course, the configurations of the images depend on the mass distribution of the lens and on the alignment of the source, lens and observer.

To summarize, the critical curves and caustics allows one to understand qualitatively the geometry of the lens mapping. We saw that they divide the lens plane into regions of positive parity ($\mu > 0$) and negative parity ($\mu < 0$). Moreover, we saw also that the caustics (corresponding to the mapping of the critical curves into the source plane) divide the source plane in regions of different image multiplicity. An important property is that the number of images change by ± 2 across a caustic and this number of images is always odd. This postulate is called the *Odd-Number Theorem*. The demonstration of this theorem is outside the framework of this thesis, but it states that the total number of images is odd and that at least one of the images corresponds to a minimum of τ (the Fermat potential).

According to what has been said before, a source which is very misaligned with the lens has one image that corresponds to a minimum of τ and if this source crosses a caustic, its number of images increases by 2. Hence, the number of images will be always odd.

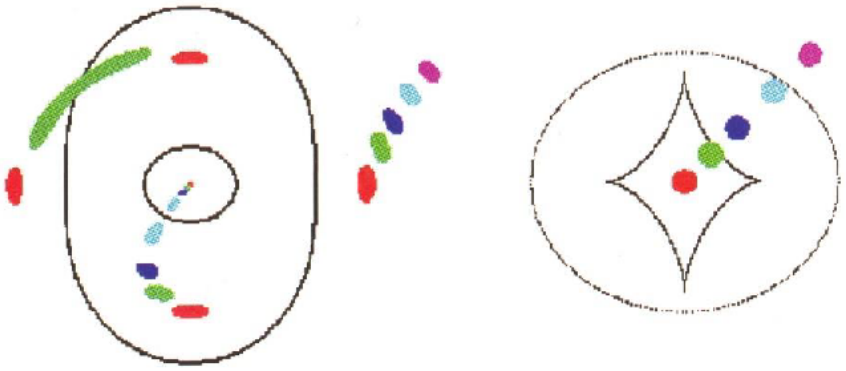

Figure 2.5: Images positions for an elliptical lens in a fold configuration [13]. The images and the critical curves (in the lens plane) are sketched on the left panel, while the source and the caustics (in the source plane) are illustrated on the right panel. The positions of the images for a source crossing a fold caustic are represented with different colors in order to see how the images evolve with respect to the source position. Similarly, the source is considered spherical with a finite extent and, when the source crosses a caustic from the "inner side" to the "outer side", this leads to the merging of three images into one. The central highly attenuated images are sketched as tiny points near the center of the lens galaxy.

"

Chapter 3

Gravitational lens modelling

In the previous chapter, one introduced the theoretical aspects of gravitational lensing. Of course, one must now put it into practice. The aim of this chapter is to learn how to infer information about the mass distribution of the lens based on the images. For this purpose, one proceeds to lens modelling, which consists in fitting mass distribution to observed data. In this chapter, the techniques to constrain lens models with different kinds of data and the main concepts of lens modelling will be introduced. The software used to accomplish this is a package called *gravlens*. It is composed of two applications, one application called *gravlens* and the other one called *lensmodel*. The *gravlens* application allows to emulating lenses, while *lensmodel* allows to fitting models to data. This chapter is based on [8, 10], provided by C. Keeton who developed the software.

3.1 Solving the lens equation

In the former chapter, the lens equation (2.7) has been introduced. Nonetheless, one may rewrite it, using (2.12) in cartesian coordinates such as $\boldsymbol{x}$ is the two-dimensional vector defining the image position in the image plane and $\boldsymbol{u}(\boldsymbol{x})$ the two-dimensional vector expressing the source position in the source plane :

$$\boldsymbol{u}(\boldsymbol{x}) = \boldsymbol{x} - \nabla\psi(\boldsymbol{x}) \; . \tag{3.1}$$

The main issue with this equation is to read it from left to right and thus finding the positions of the image(s) by selecting the position of the source. The difficulty comes from the fact that the scaled deflection angle $\boldsymbol{\alpha} = \nabla\psi$ is not always solvable analytically or does not always contain simple algebraic functions. Moreover, even numerical solutions are hard to obtain since no existing algorithm provides every time all the roots of a two-dimensional equation [17]. Thus, to solve the lens equation numerically, the

number of images as well as their approximated positions must be known. This is the case for simple lens models which display a symmetrical shape, the general knowledge of their critical curves and caustics allows one to resolve numerically the lens equation and to find the positions and the number of images. However, for more sophisticated lens models, such as galaxies with companions and satellites or when there are several galaxies along the line of sight, the caustic structure is difficult to evaluate. Hence, there is a need for a generic algorithm which does not necessitate symmetry hypotheses.

The idea is to inverse the reading direction of the lens equation (3.1), thus reading it from right to left. Therefore, the goal is to make a mapping from the image plane to the source plane, taking each image position $\boldsymbol{x}$ and mapping it to a (unique) source position $\boldsymbol{u}(\boldsymbol{x})$. In fact, the concept of this procedure is to set a tiling in the image plane and to match it with the corresponding tile in the source plane. This can be done by mapping each tiles intersection (in the image plane) using the lens equation, thereby obtain a source plane that is tiled and in which every point is covered by at least one tile. Thanks to this process, the lens equation can be solved in any case.

An example of the tiling which has just been described is represented in Figure 3.1, where one considers a nearly circular lens model. The tiled image plane is distorted and folded by the lens mapping leading to the tiling of the source plane. The overlaps of the tiling in the source plane gives regions where multiple imaging is possible. In other words, if a source lies in a region where tiles overlap, the result is that there are multiple images in the image plane situated on tiles corresponding to the ones that overlap in the source plane. Indeed, each tile of the source plane corresponds to a unique tile that is mapped in the image plane. Hence, it is the fact that a source is located in a region related to more than one tile which leads to multiple solutions of the lens equation and thus, multiple imaging.
This is well illustrated in Figure 3.1, where the three images (the central image is hard to see because the tiling is compact), represented by a triangle, a disc and a square, all correspond to a unique position of the source. Moreover, the heavy curves in the image plane are the critical curves which are mapped into caustics in the source plane.

Consequently, the tiling method has plenty of advantages, it allows one to know the number of images and their approximate positions which can then be improved with a numerical root finder. Furthermore, there is no need to know the symmetry of the lens, the tiling algorithm is able to solve the lens equation for all mass distributions and lens configurations.

Furthermore, the question of the resolution of the tiling remains to be addressed. On Figure 3.2, on the left panel, a section tiling in the image plane is represented and one

can see that the tiling is much more accurate near the critical curve (the heavy curve). Indeed, to improve the resolution, i.e. in order to obtain more precise source or images positions, the idea is to divide the tile into sub-tiles. Then, these sub-tiles are mapped onto the source plane, leading to a better resolution for the source position and images positions.

In addition, on Figures 3.1 and 3.2, one can see that the image plane is actually folded on the critical curve, then the projection onto the source plane can be done, leading to the mapping of the caustic as shown on the right panel of the Figure 3.2. The vertices of the section tiling are marked by triangles and squares, they allow to realize how the folding is executed. Indeed, the bottom figures do not lie in the same place, showing that the tiles below the critical curve are kind of returned by the mapping towards the source plane. One may add that the sub-tiling is in fact useful to resolve the folding near the critical curves, it allows also to put bounds on the location of the critical curves, that can be thereafter precised with a numerical root finder.

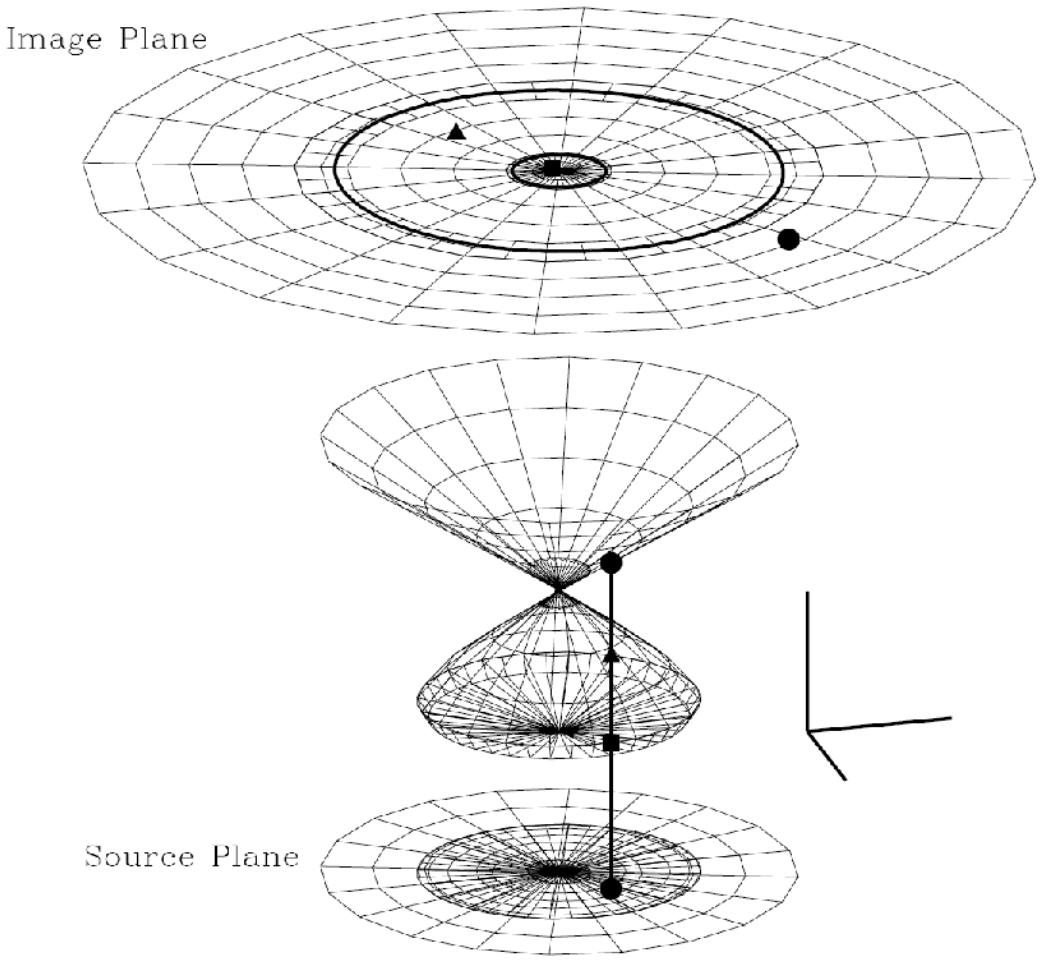

Figure 3.1: Representation of the tiling from the image plane to the source plane [10].

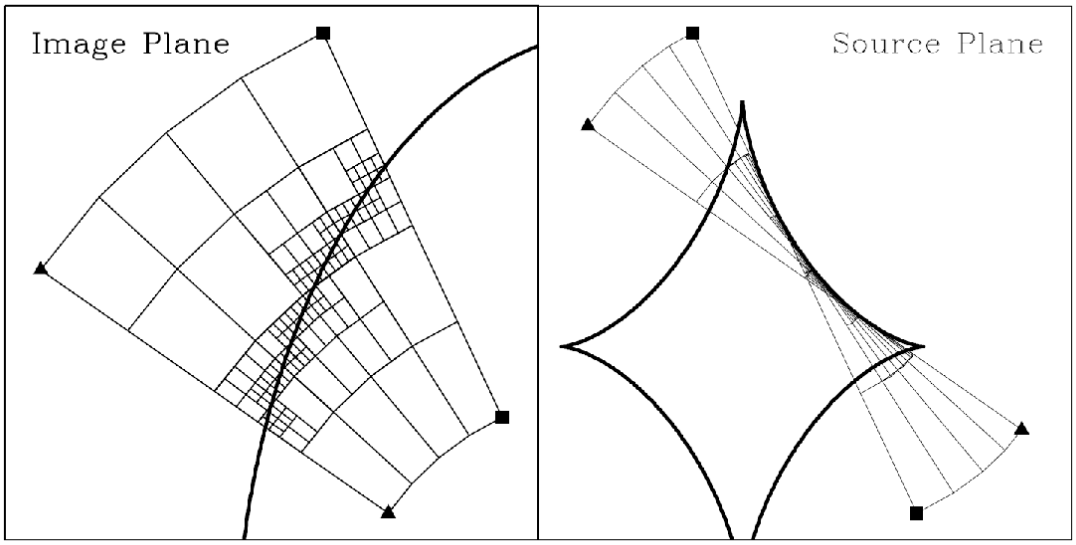

Figure 3.2: Sample tiling near a fold caustic [10].

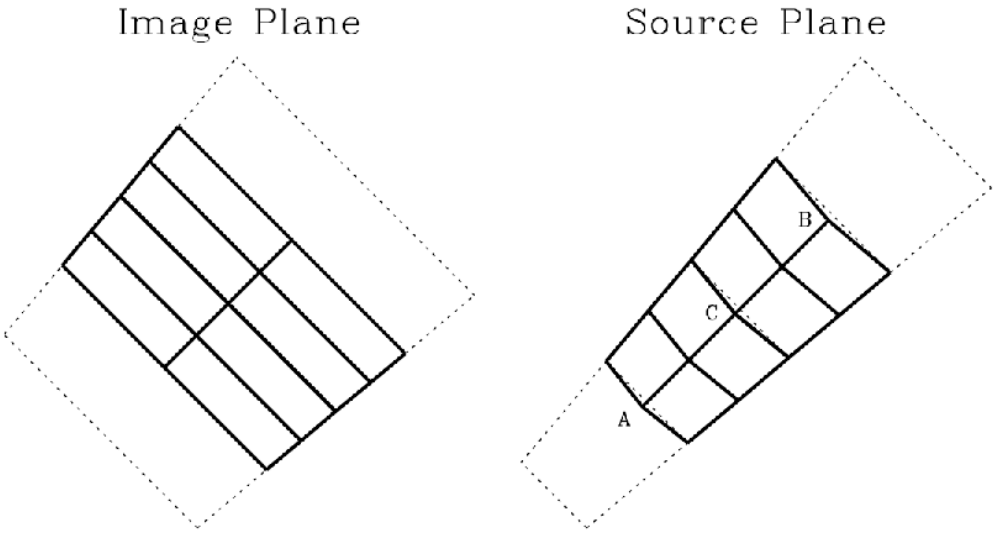

Figure 3.3: Sample tiling with four tiles, where two have 2 x 2 sub-tiling [10].

Finally, in Figure 3.3, four tiles are represented and two are subdivided in a 2 x 2 sub-tiling. The dotted lines are for the main tiling and the solid lines represent the sub-tiling. In such a configuration, when the resolution changes for adjacent tiles in the image plane, it may result in a gap (point B) or an overlap (point A) for the corresponding tiles in the source plane. Actually, it is due to the fact that a straight line in the image plane can be mapped as a curve into the source plane. However, if, the adjacent tiles are themselves sub-tiled, the gap produced in a sub-tiling is compensated by the overlap of another sub-tiling (point C). The problem appearing when the resolution between tiles is not the same, resulting in a overlap or a gap, can be easily solved using a 2 x 2 sub-tiling because they form a triangle that can be examined. In fact, the quadrilaterals forming either the tiling or the sub-tiling are usually divided into two triangles because triangles are the only polygons that remain convex even when they are deformed by the mapping. Therefore, triangles are much easier to analyse and they are used in every tiling or sub-tiling, particularly when there is a gap or an overlap between tiles.

To summarize, the tiling algorithm qualitatively presented in this section allows the making of a mapping of the image plane towards the source plane without the need to resolve analytically the expression of the deflection potential $\nabla\psi$ because it can be easily calculated thanks to the tiles for a given mass distribution κ by (2.11) and (2.12). The mapping provides the caustics in the source plane and gives the opportunity to solve the lens equation (3.1) from left to right, i.e. to find the positions of all images for a given source position. A different tiling can be created for each mass distribution and lens configuration, even the more complicated ones. This algorithm is implemented in the *gravlens* software and will be used in the modelling subsequently introduced in order to generate a gravitational lens system and in order to fit the positions of the images in the lens plane.

3.2 Lens modelling

The aim of lens modelling is to infer information about the lensing galaxy. For this purpose, one needs firstly to choose a mass distribution and then to find the parameters of the mass distribution that allow reproducing the lens system. In the *lensmodel* application, there are various canonical models included in the code. A canonical model corresponds to a mass distribution that has an ellipsoidal symmetry and this kind of relatively simple model allows the lens equation to be solved without difficulty. In other words, with a canonical model, the lens equation (3.1) can be solved from right to left because the expression of the deflection potential $\nabla\psi$ can be easily calculated and thus, the tiling introduced in the previous section can be established.

A relevant mass model for strong gravitational lensing involving one galaxy is the *softened power law model*. This model includes the simple isothermal models with density $\rho \propto r^{-2}$, but allows the central singularity appearing when $r \to 0$ to be eliminated. To that end, the *softened power law model* incorporates a core radius with a finite density and thus, the lens center is made of a core region where the central singularity is no more permitted [15, 21]. Furthermore, the *softened power law model* includes also an external shear. Indeed, a (real) galaxy is never completely isolated and undergoes the influence of surrounding objects. This external shear is not related to the mass of the lens but impacts the deflection potential which is kind of stretched in a direction and flattened in another. Therefore, it depends on a position angle that determines its direction [21].
The density profile of the softened power law model is written [8] :

$$\kappa = \frac{1}{2}\left(b'\right)^{2-\alpha}\left[\left(s'\right)^2 + \zeta^2\right]^{\alpha/2-1}, \tag{3.2}$$

where κ is the convergence or dimensionless surface mass density (2.10) and the 9 parameters appearing either in the equation or describing this model are given in Table 3.1. Moreover, $\zeta = \left[(1-\varepsilon)x^2 + (1+\varepsilon)y^2\right]^{1/2}$ is the elliptical radius, where ε is related to the axis ratio by $q^2 = (1-\varepsilon)/(1+\varepsilon)$.

Parameter	Signification
b'	Mass scale
x	Abscissa of the galaxy position
y	Ordinate of the galaxy position
e	Ellipticity
θ_e	Position angle of the ellipticity
γ	External shear
θ_γ	Position angle of the external shear
s'	Core radius
α	Power law index

Table 3.1: Parameters of the softened power law density model [8].

Some comments about this table must be made. b' is, in some way, the "strength" of the lens, it is used to express the mass density of the lens model. x and y are the Cartesian coordinates of the lens (with respect to an arbitrary origin, most of time the center of the field of view). e is the standard ellipticity $e = 1 - q$, with $q = b/a$, the axis ratio. θ_e and θ_γ are measured from the "North axis", counter clockwise. γ and e are dimensionless and do not influence the radial density profile. By contrast, s', which is related to the scale dimensions of a flat core radius [9], affects the density profile, but will not be used and thus, set to zero throughout all my modellings (this kind of model is called "singular" and it is possible only if $\alpha > 0$) [9]. Finally, α is of significant importance, this parameter governs almost by itself the density profile.

Once the lens mass model is chosen, the goal is to find the parameters of the mass distribution that allow reproducing the lens system. In other words, one proceeds with a fit to find the values of the lens parameters that match best the observed data by resolving the lens equation (3.1).
To do so, the strategy is to start with arbitrary parameters and try to fit this first model to the observed data. The quality of the fits is expressed by the χ^2 and a good fit is achieved for a low χ^2. Most of time, the data available are the images positions, the images fluxes

and the time delays between the images. A χ^2 is calculated by the software *lensmodel* by comparing the observed and predicted values of the observables (ponderated by the error), such that the χ^2 can be easily split for each observable individually. Thus, progressively, the model can be refined and the fitted data become closer and closer from the observed ones. When one considers that the χ^2 of the model is sufficiently low, i.e. when the reduced χ^2 is close to 1, one can establish the density profile of the observed lens with the relation (3.2).

An important aspect about the fitting method deserves to be reported. The usual χ^2 relating to the images positions is χ^2_{img} and it is calculated in the image plane, i.e. by comparing the observed images positions and the images positions derived from the model and evaluated thanks to the tiling. Nonetheless, it can be replaced by χ^2_{src}, which is related to the source position and calculated in the source plane. By using this alternate position χ^2 examined in the source plane, the lens equation (3.1) does not need to be solved with the tiling. Indeed, it is solved immediately from right to left, using the observed images positions and the fitted mass distribution, thus giving the "observed source position" (strictly speaking, it is not an observable, but rather a result of the data and the fitted mass distribution). The χ^2_{src} is obtained by comparing the "observed source position" and the "model source position". The model source position is in fact, in a way, a parameter of the mass model since it is retrieved based on the parameters of the model, calculating the source position for each "observed" image and rescaling their error bars based on the magnification matrix. The model source position can be easily fitted for a given mass model because its best solution that minimises the χ^2 can be evaluated analytically (see [10] for more details). The advantage of such a χ^2_{src} method is that the fit is performed more rapidly than with χ^2_{img} because the tiling does not need to be implemented by the software. However, χ^2_{src} is just an approximation of χ^2_{img}. It can be used in a initial modelling, in order to explore the space parameter, but once a relatively good model is found, the χ^2_{img} method must be applied to refine the model and try to find the best-fit parameters.

In the modelling of the forthcoming chapters, firstly, one evaluates the χ^2_{src} in the source plane by proceeding with a "randomization", i.e. generating a set of models with random values of the parameters allowed to vary in a specified space parameter and then an optimization algorithm is applied. After that, an optimization algorithm using χ^2_{img} in the image plane is performed on the best model found in the source plane, providing the lens parameters that one wanted to infer [8].

Chapter 4

A first model

In this chapter, a first modelling will be presented, emphasizing the importance of the mass distribution that is considered and the degrees of freedom attributed to the model. The results of the fits will be examined and interpreted, in order to understand how the *lensmodel* application works and how the model parameters of the lens react to the constraints imposed.

To illustrate the modelling procedure, one creates simulated lens systems that one will subsequently model.
Firstly, a mass distribution for the lens must be specified, one chooses the *softened power law density model* as introduced in the previous chapter. The density profile of this model is given by the equation (3.2) and its parameters are introduced in Table 3.1.
Secondly, the images must be generated. To that end, one uses a function of the software called *findimg* [8] that solves the lens equation (3.1) for a given source position and returns the coordinates of the images, their fluxes and their time delays. In other words, this function proceeds to the mapping from the source plane to the image plane, thanks to the tiling algorithm developed in the previous chapter.

Now that this artificial gravitational lensing system is created, it can be modeled and fitted as explained in Section 3.2. The aim of this chapter is to see how the fit changes when different parameters of the lens are allowed varying or when noise is added on the data and then, try to interpret the obtained results.

4.1 Method

The coordinates of the source are chosen so that three types of lensing configuration with four images will be generated: a cusp, a fold and a cross configuration. The cusp and fold configurations have already been introduced in the Figures 2.4 and 2.5. The cross configuration simply corresponds to a source situated in the center or very close to the center of the two caustics, resulting in four images arranged in a cross (if the faint central image is not taken into account). The latter configuration is in fact represented in red in the Figures 2.4 and 2.5.

To implement the function *findimg*, one must state in input the red-shifts of the source and the lens, the Hubble constant (needed to derive proper delays), cosmological density parameters, as well as arbitrary parameters for the lens. The mock lens is created with basic properties similar to the galaxy extracted from hydrodynamical simulations that will be modeled in the next chapter. For this purpose, one sets the source redshift $z_{src} = 2.0$, the lens redshift $z_{lens} = 0.271$ and a cosmological world model with $H_0 = 70 kms^{-1}Mpc^{-1}$, $\Omega_M = 0.31$ and $\Omega_\Lambda = 0.69$. The three different configurations of images are generated with the same mock lens parameters, presented in Table 4.1. Nonetheless, note that those parameters are not fixed completely arbitrarily, they are in fact quite similar to those obtained after the modelling of the lens system presented in the next chapter.

b'	x	y	e	θ_e	γ	θ_γ	s'	α
1.9	0.0	0.0	0.5	-65.0	0.0	0.0	0.0	1.2

Table 4.1: Parameters of the lens to generate the lens system.

For each configuration, four different fits were made, starting with the same mass model parameters used to generate the system, introduced in Table 4.1. In those fits, b', e, γ and α are always set as free parameters with rather small ranges of variation because the mass model is kind of already known. The first fit, denoted **1**, is a noiseless one and consists in letting the position angle of the ellipticity θ_e and the position angle of the shear (θ_γ) vary. The three other fits include some noise on their data and aim to study the impact on the results and the capacity to obtain a good χ^2 when the constrains are progressively released and the model gradually refined. Therefore, in the second fit (**2**), only the four parameters mentioned before can vary, while for the third fit (**3**), the position angles θ_e and θ_γ are also stated as free parameters. Finally, the fourth fit (**4**) is the same as the third one, but the centroid of the lens (x and y) is free to vary.

The noise that is added on the data is a Gaussian noise, hence depending on the uncertainties on these data. The uncertainty is set at 0.003 arcsec for the positions of the images, 20% for the flux ratios and 2% for the time delays. The large uncertainty of the flux ratios is due to the fact that, in a real gravitational lensing system, the luminosity of the source can be fluctuating and, combined with time delay, it could lead to significant errors in the measurements of the flux ratios. In addition, microlensing effects by objects in the lens galaxy could also lead to substantial errors for the fluxes [8]. The uncertainty on the images positions is too low for optical telescopes, but is achievable for high precision measurements in the radio domain. Hence, one uses this uncertainty in order to make the strongest possible constraints on the model [6].

Moreover, the data provide 14 constraints: 2 for the galaxy position (stated at (0,0) with an uncertainty of 0.25 arcsec), 6 for the images positions (measured with respect to the position of one image), 3 for the flux ratios (with respect to one image) and 3 for the time delays (again with respect to one image, "the first incoming" image). The *softened power law model* used here includes 8 parameters and not 9 because one considers a singular model, *s'* relating to the core radius is fixed to 0. The number of degrees of freedom changes depending on the number of parameters that are fitted.

4.2 Cusp configuration

The results of the fits for the cusp configuration are presented in Tables 4.2 and 4.3.
The Table 4.2 shows how the parameters of the lens galaxy vary with the different fits mentioned above (**1**, **2**, **3** and **4**). It can be seen that those parameters do not vary a lot. Nonetheless, the addition of the noise on the data and the freeing of the position angles (**3**) leads to a non-negligible shear (γ) and a little variation of α. The most noticeable result is, of course, for the fit **4**, when the centroid is set as a free parameter. Indeed, the ellipticity (e) is smaller than those of the other fits as well as b' and α which have also changed rather significantly. The value of the parameters for the fit **4** can seem strange, but, as showed in Figure 4.1, they correspond to a global minimum in terms of χ^2. Therefore, the freeing of the centroid allowed the model to match better with the noised data by moving a little bit away from the expected parameters.

The consequences of the addition of the noise is perceptible in the augmentation of the χ^2 pointed out in the Table 4.3 for the fits **2**, **3** and **4** in comparison with the fit **1**. Moreover, it can be seen that the progressive freeing of parameters in the fits **3** and **4** leads to the diminution of the χ^2 and this can simply be explained by the observables being better returned when the model has more freedom in its parameters and thus, it can adapt better to the data. Furthermore, one can notice that the decrease of the χ^2 between

the fits **2** and **3** is due to the χ^2 of images positions which has decreased because of the freeing of the position angles. Finally, the χ^2 relative to the position of the lens galaxy (**gal**) is clearly negligible.

	b'	*x*	*y*	*e*	θ_e	γ	θ_γ	*s'*	α
1	1.9	(0.0)	(0.0)	0.5	-65.0	0.0	-64.737	(0.0)	1.2
2	1.901	(0.0)	(0.0)	0.499	(-65.0)	0.0	(0.0)	(0.0)	1.202
3	1.893	(0.0)	(0.0)	0.498	-64.866	0.012	-68.063	(0.0)	1.175
4	1.951	-0.022	0.053	0.414	-64.551	0.016	-69.856	(0.0)	1.25

Table 4.2: Comparison of the fitted lens parameters for the cusp configuration. The parameters into brackets are fixed and the values are rounded to the third decimal.

	tot	**pos**	**flux**	**tdel**	**gal**	**dof**
1	1.847e-04	1.788e-06	1.829e-04	3.482e-09	0.000e+00	8
2	3.480e+00	2.519e+00	8.100e-01	1.508e-01	0.000e+00	10
3	1.076e+00	2.529e-02	8.938e-01	1.575e-01	0.000e+00	8
4	8.651e-01	1.061e-03	6.350e-01	1.767e-01	5.240e-02	6

Table 4.3: Comparison of the χ^2 for the cusp configuration, with the degrees of freedom in the last column.

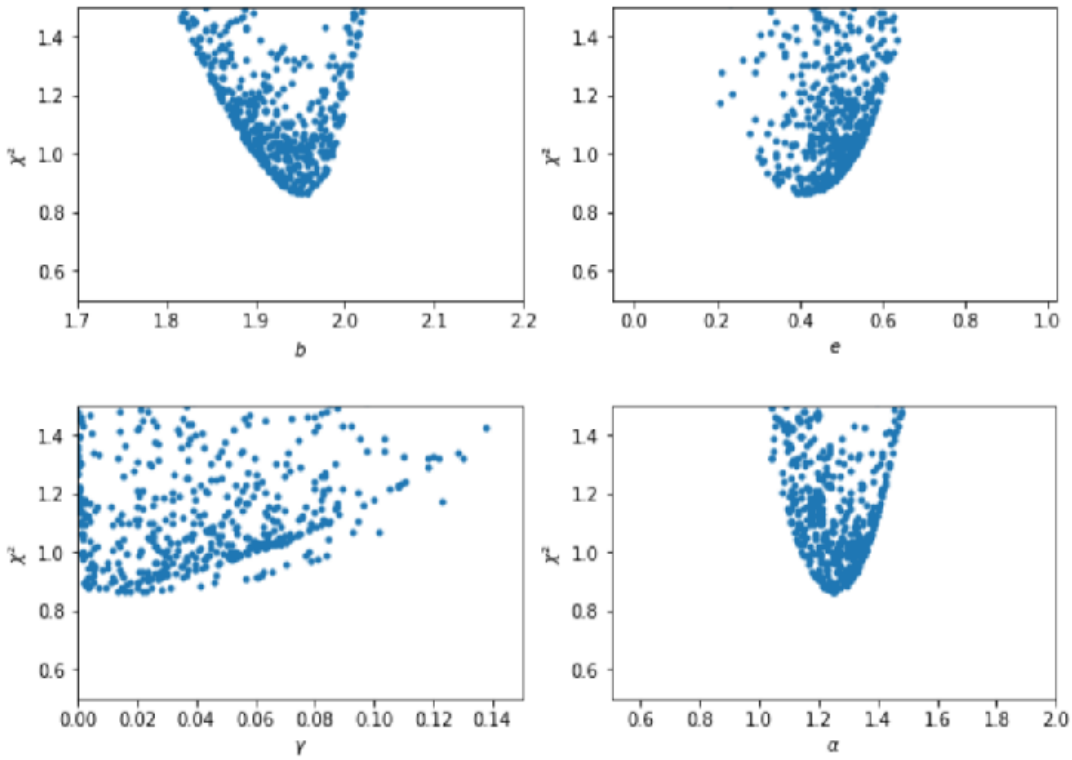

Figure 4.1: Total χ^2 plots for the fit **4** of the cusp configuration, evaluated in the source plane, with respect to the parameters b', e, γ, and α.

4.3 Cross configuration

For the cross configuration, the statements about the parameters presented in Table 4.4 are the same as those made for the cusp configuration for the fits **1** and **2**. Nonetheless, the fit **3** is quite different, the ellipticity (e) has increased, the shear (γ) is much larger and its position angle θ_γ is substantially offset with respect to the semimajor axis of the lensing galaxy. These rather curious results could be explained considering that a degeneracy exists between e and γ. However, since α has also significantly changed, this explanation does not appear to be valid because the shear could try to accomodate for the excess/default of mass induced by the change of the slope [22]. The χ^2 plots with respect to the parameters of interest for the fit **3** are showed in Figure 4.2 and one observes that the best fitted model corresponds to a global minimum of χ^2. Thus, all these results could be explained by the fact that the centroid is not free, hence the model has to notably change its parameters to recover the data. Effectively, it can be seen on the fit **4** that the parameters retrieve values much closer than previously, when the position

of the lens center can be modified.

	b'	x	y	e	θ_e	γ	θ_γ	s'	α
1	1.899	(0.0)	(0.0)	0.5	-65.0	0.001	-65.0	(0.0)	1.197
2	1.896	(0.0)	(0.0)	0.508	(-65.0)	0.001	(0.0)	(0.0)	1.191
3	1.920	(0.0)	(0.0)	0.572	-64.820	0.148	25.285	(0.0)	1.446
4	1.875	0.007	0.004	0.523	-64.790	0.017	-66.575	(0.0)	1.131

Table 4.4: Comparison of the fitted lens parameters for the cross configuration. The parameters into brackets are fixed and the values are rounded to the third decimal.

The considerations about the χ^2 presented in Table 4.5 are the same as those made for the cusp configuration for the fits **1** and **2**. In addition, the χ^2 relative to the images positions of the fit **3** is smaller than the one of the fit **2**, but still rather "high". It illustrates what has been mentioned just before, the model could have experienced difficulties to retrieve the correct images positions because the centroid was not free and had to change its parameters to match with the data in the best possible way. Therefore, sometimes, adding freedom to the system facilitate to recover better data, but can lead to bias on the fitted parameters if there remain other constrains on the model.

	tot	**pos**	**flux**	**tdel**	**gal**	**dof**
1	5.700e-04	1.092e-05	5.586e-04	4.929e-07	0.000e+00	8
2	5.949e+00	4.996e+00	8.782e-01	7.478e-02	0.000e+00	10
3	3.755e+00	2.307e+00	1.315e+00	1.322e-01	0.000e+00	8
4	1.217e+00	1.801e-02	8.465e-01	3.519e-01	9.594e-04	6

Table 4.5: Comparison of the χ^2 for the cross configuration, with the degrees of freedom in the last column.

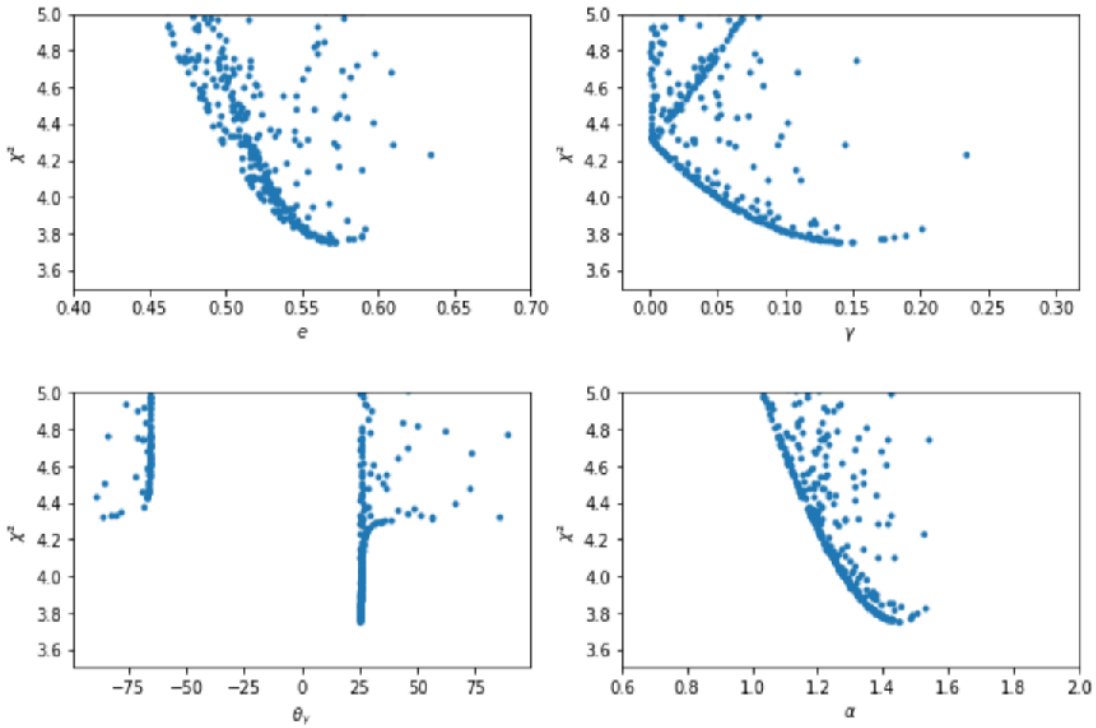

Figure 4.2: Total χ^2 plots for the fit **3** of the cross configuration, evaluated in the source plane, with respect to the parameters e, γ, θ_γ and α.

4.4 Fold configuration

The fits for the fold configuration tell us nothing new in terms of χ^2 (Table 4.7) and parameters (Table 4.6), excepted the fact that the shear γ and its position angle θ_γ are quite different between the fits **3** and **4**. One can see on the χ^2 plots of the fit **4** (Figure 4.3) that θ_γ do not converge clearly towards a minimum of χ^2, compared to the χ^2 plot of γ that shows a global minimum. This could explain the value of the position angle of the shear, which is quite different for the different fits.

	b'	x	y	e	θ_e	γ	θ_γ	s'	α
1	1.9	(0.0)	(0.0)	0.5	-65.001	0.0	-52.609	(0.0)	1.2
2	1.903	(0.0)	(0.0)	0.496	(-65.0)	0.0	(0.0)	(0.0)	1.203
3	1.887	(0.0)	(0.0)	0.510	-65.451	0.005	-42.343	(0.0)	1.181
4	1.905	-0.030	-0.024	0.471	-65.246	0.021	-62.049	(0.0)	1.180

Table 4.6: Comparison of the fitted lens parameters for the fold configuration. The parameters into brackets are fixed and the values are rounded to the third decimal.

	tot	**pos**	**flux**	**tdel**	**gal**	**dof**
1	5.547e-04	8.475e-06	5.461e-04	1.304e-07	0.000e+00	8
2	3.579e+00	2.063e+00	1.189e+00	3.268e-01	0.000e+00	10
3	1.905e+00	1.020e-01	1.198e+00	6.045e-01	0.000e+00	8
4	1.479e+00	2.023e-03	1.150e+00	3.034e-01	2.344e-02	6

Table 4.7: Comparison of the χ^2 for the fold configuration, with the degrees of freedom in the last column.

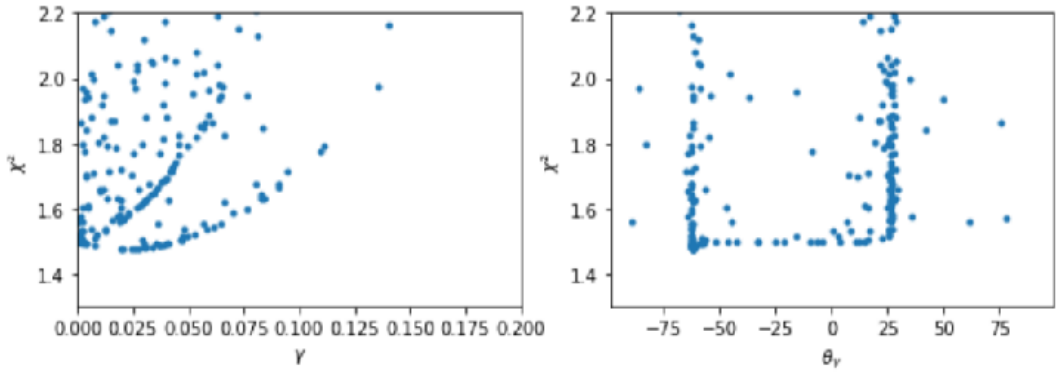

Figure 4.3: Total χ^2 plots for the fit **4** of the fold configuration, evaluated in the source plane, with respect to the parameters γ and θ_γ.

It is important to emphasize the fact that the total χ^2 of the three configurations presented in the tables above are rather low, but are not the reduced χ^2. If one divides those total χ^2 by the number of degrees of freedom (dof) to obtain the reduced χ^2, one realizes that it is < 1 for all models. This may reflect the fact that the models fit improperly the noise on the data or the fact that the uncertainties have been overestimated. For the noiseless fit **1**, it is clear that the uncertainties are overestimated, while for the fits with noisy data,

these two explanations can be valid since the model is fitted starting with the parameters that are used to generate the lens system. Actually, the lens parameters are generally relatively well retrieved for all configurations.

Finally, one may also want to see how well the Einstein radius and the Hubble constant are retrieved by those simple models, depending on the image configuration. In Table 4.8, it can be seen that the fitted H_0 is relatively close to the value used to generate the lens system ($70 kms^{-1}Mpc^{-1}$) throughout all the fits, except for the fit **3** of the cross configuration and the fit **4** of the cusp configuration. For the fit **3** of the cross configuration, this could be explained by the fact that, as already mentioned, the fitted model is not very convincing and seems to be biased, resulting also in a biased value for H_0. For the fit **4** of the cusp configuration, the rather small value of H_0 could be explained by time delays that are not well retrieved. Indeed, as shown on Table 4.3, the χ^2 relating to the time delay of the fit **4** is the largest of all the fits. The Einstein radius θ_E (Table 4.9) is also quite constant throughout all the fits, except again for the fit **3** of the cross configuration, but the explanation can be the same as for the Hubble constant.

	Cusp	Cross	Fold
1	69.99	70.16	69.99
2	69.24	69.76	69.77
3	70.78	55.19	72.64
4	59.56	75.01	68.91

Table 4.8: Hubble constant (H_0) fitted for each fit and configuration, in $kms^{-1}Mpc^{-1}$.

	Cusp	Cross	Fold
1	2.050	2.049	2.050
2	2.050	2.052	2.050
3	2.042	2.118	2.046
4	2.043	2.048	2.034

Table 4.9: Einstein radius (θ_E) fitted for each fit and configuration, in arcsec.

A few additional remarks about the fits deserve to be mentioned. For the modelling that are noiseless, one can expect the χ^2 to be equal to zero. However, the χ^2 relating to fit **1** are very low, but not equal to zero. In fact, the difference is dominated by numerical uncertainties, these results are compatible with a χ^2 equal to a zero value.

Furthermore, one has seen that the parameters of the cross configuration are less accurately retrieved than the ones of the other configurations, for the noisy data and when the position angles are free to vary (fit **3**). This could be explained by the fact that, to obtain a cross configuration, the alignment between the lens and the source must be almost perfect and the images positions are very sensitive to the source position [18]. Hence, to better match with the noisy images positions for a centroid that is fixed, the model has to modify the shape of the caustics by considering a non-negligible external shear γ and an unexpected value for the position angle θ_γ specifying its direction. The shape of the caustics is modified because, even if the lens is symmetric, the corresponding deflection potential can be asymmetric due to the influence of external masses near the lens or along the line of sight, resulting in a mapping of the caustics that differs from the one of the isolated symmetric lens [21]. Then, once the centroid of the lens is liberated, the parameters recover values much more in adequacy with the results modeled in the other configurations since the model do not need to include a high γ to retrieve correctly the images positions.

To conclude, the mock lenses generated and modeled in this section allowed one to quantify the ability of the modelling to retrieve the lens properties, when the lens potential is smooth and axisymmetric. In fact, this first approach is interesting for the purpose of this thesis because it allows one to understand how the models behave when different configurations of gravitational lensing are implemented and when free parameters are added or removed, depending on the complexity of the lens model.

Chapter 5

Modelling of a mock lens from hydrodynamical simulations

In this chapter, the modelling of a mock lens galaxy from hydrodynamical simulations, i.e. a numerical simulation of a galaxy including dark-matter as well as baryonic components, is performed. The lens galaxy is created within the framework of the EAGLE project (Evolution and Assembly of GaLaxies and their Environment) [1], which is a suite of hydrodynamical simulations of the formation of galaxies and super-massive black holes in a ΛCDM universe. Then, the mock lens system is generated with a modified version of the SEAGLE pipeline (Simulating EAGLE LEnses), which is a pipeline used to simulate and to model strong lenses [14]. The modified version of the pipeline is the result of the PhD work of Lyne van de Vyvere. The main difference with respect to SEAGLE is in the ray-tracing of the source, which is now based on the lenstronomy code [2].

Three gravitational lensing systems corresponding to the cusp, fold and cross configurations are simulated with the same mock lens galaxy thanks to the pipeline (Figures 5.1, 5.2 and 5.3). One disposes of the data belonging to these three systems (point images positions, flux ratios and time delays), as well as the projected mass map (κ map) of the lens galaxy represented on Figure 5.4.
The uncertainties on the observed data are once again set at 0.003 arcsec for the images positions, 20% for the flux ratios and 2% for the time delays and a Gaussian noise is added on the data of all fits in the same manner as in the previous chapter.

The aim of this chapter is to infer the mass distribution of the lens galaxy by fitting its parameters to the observed data in order to test if an analytical mass model can reproduce the properties of a non-analytic (or realistic) lens.

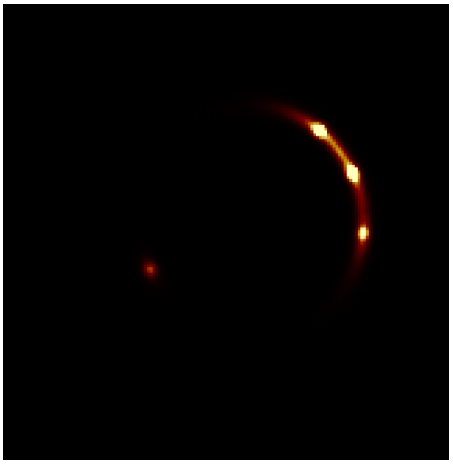

Figure 5.1: Simulated gravitational mirage in a cusp configuration, generated with the modified pipeline [14].

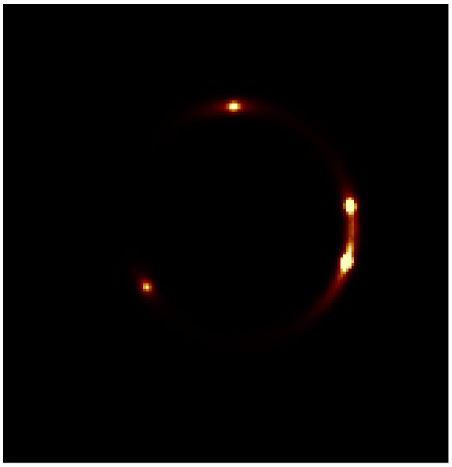

Figure 5.2: Simulated gravitational mirage in a fold configuration, generated with the modified pipeline [14].

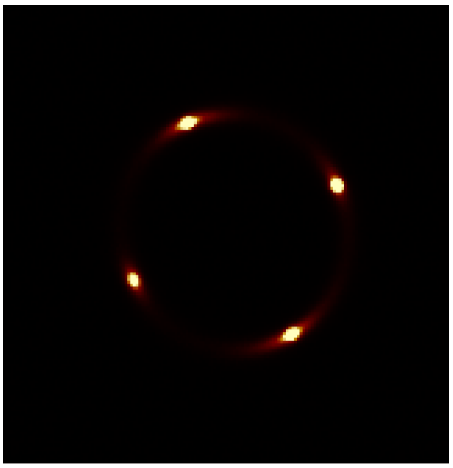

Figure 5.3: Simulated gravitational mirage in a cross configuration, generated with the modified pipeline [14].

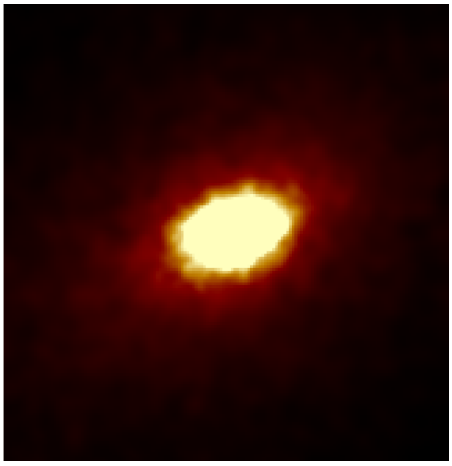

Figure 5.4: κ map of the mock lens, generated with SEAGLE [14], on the basis of the galaxy created with the EAGLE project [1].

5.1 Methodology

The mass model that is fitted is once again the softened power law mass distribution (3.1), without core radius (*s'*=0). The starting parameters for the modelling of the three lensing configurations are unimportant here compared to the previous chapter because the mass distribution of the lens is completely unknown. Hence, the ranges of variation of those parameters are very large in the beginning of the fitting process. Moreover, the values of the cosmological parameters and the redshifts of the lens and the source are also the same as the ones used previously in order to match with the cosmological world model used in EAGLE: $\Omega_M = 0.31$, $\Omega_\Lambda = 0.69$, $z_{src} = 2.0$, $z_{lens} = 0.271$ and H_0, which is implemented only if the time delays are not constrained, is stated equal to $67.7 kms^{-1}Mpc^{-1}$.

The fitting method is essentially the same as the one introduced in the previous chapter. One proceeds with a randomization in the source plane and then with an optimization in the image plane. However, the different fitting steps are not the same, the constraints and the free parameters of each fit are not managed in a similar manner as previously and the ranges of variation of the parameters are quite large in the beginning because one has no idea about their value.
One starts with fitting all the observed data to all lens parameters, except *s'* and the power law index α which are fixed in the randomization and the optimization (fit **1**).
Then, the fit **2** is performed and it is the same as the previous one, but the time delays are not considered as constraints.
In the fit **3**, the time delays are once again not stated as constraints and for the randomization in the source plane, α is set as a free parameter as well as *b'*, *e* and γ, but the other parameters are fixed. However, for the optimization in the image plane, all the parameters are liberated (except *s'*).
The fit **4** involves the same procedure as the fit **3**, although this time, the time delays are included into the constraints.
To conclude, the fit **5** consists in letting vary all the parameters for the randomization and the optimization (again except *s'*).

The interest of such a fitting method is to gradually refine the parameters of the lens by starting each fit with the fitted parameters of the previous fit and modifying the degrees of freedom in each of them. The methodology used for the fits **3** and **4** is justified because, as one will see, the parameters that are fixed in the randomization seem already well retrieved in the fits that precede them.

Sections 5.2, 5.3 and 5.4 provide the fitting results of the different configurations and a comparison of the results obtained for the different configurations is presented in section 5.5.

5.2 Cusp configuration

The fitted parameters for the cusp configuration with respect to the different fitting steps introduced in the previous section are presented in Table 5.1. It can be seen that the first four fits give parameters that are quite similar, although they seem to converge towards a very refined model. If one takes a look at the χ^2 in Table 5.2, one sees that the latter are mainly due to the time delays and rather equivalent in terms of reduced χ^2, which are relatively low. However, the reduced χ^2 relating to the fit **4** is the highest whereas this fit is supposed to be more accurate than the fit **1**, for which the time delays were also considered. The model could be blocked in a local minimum, but it can be seen on Figure 5.5 that the parameters are not blocked in a local minimum and converge well towards a global minimum for the randomization in the source plane of the fit **4**.

	b'	x	y	e	θ_e	γ	θ_γ	s'	α
1	1.825	-0.054	-0.085	0.538	-65.899	0.133	23.616	(0.0)	(1.0)
2	1.885	0.041	-0.042	0.468	-66.030	0.107	23.322	(0.0)	(1.0)
3	1.884	0.041	-0.042	0.469	-66.031	0.107	23.320	(0.0)	0.999
4	1.882	0.039	-0.042	0.471	-66.042	0.108	23.284	(0.0)	0.995
5	1.624	0.136	0.132	0.689	-72.950	0.080	-16.008	(0.0)	0.241

Table 5.1: Comparison of the fitted lens parameters for the cusp configuration. The parameters into brackets are fixed and the values are rounded to the third decimal.

	tot	**pos**	**flux**	**tdel**	**gal**	**dof**
1	1.466276e+01	1.016584e-01	4.615739e+00	9.784281e+00	1.610794e-01	7
2	4.655389e+00	4.054699e-02	4.560480e+00	0.000000e+00	5.436184e-02	4
3	4.655080e+00	4.052782e-02	4.560244e+00	0.000000e+00	5.430756e-02	3
4	1.484745e+01	8.195311e-02	4.527786e+00	1.018425e+01	5.346422e-02	6
5	5.444313e+00	9.447160e-03	4.131328e-01	4.449114e+00	5.726191e-01	6

Table 5.2: Comparison of the χ^2 for the cusp configuration, with the degrees of freedom in the last column.

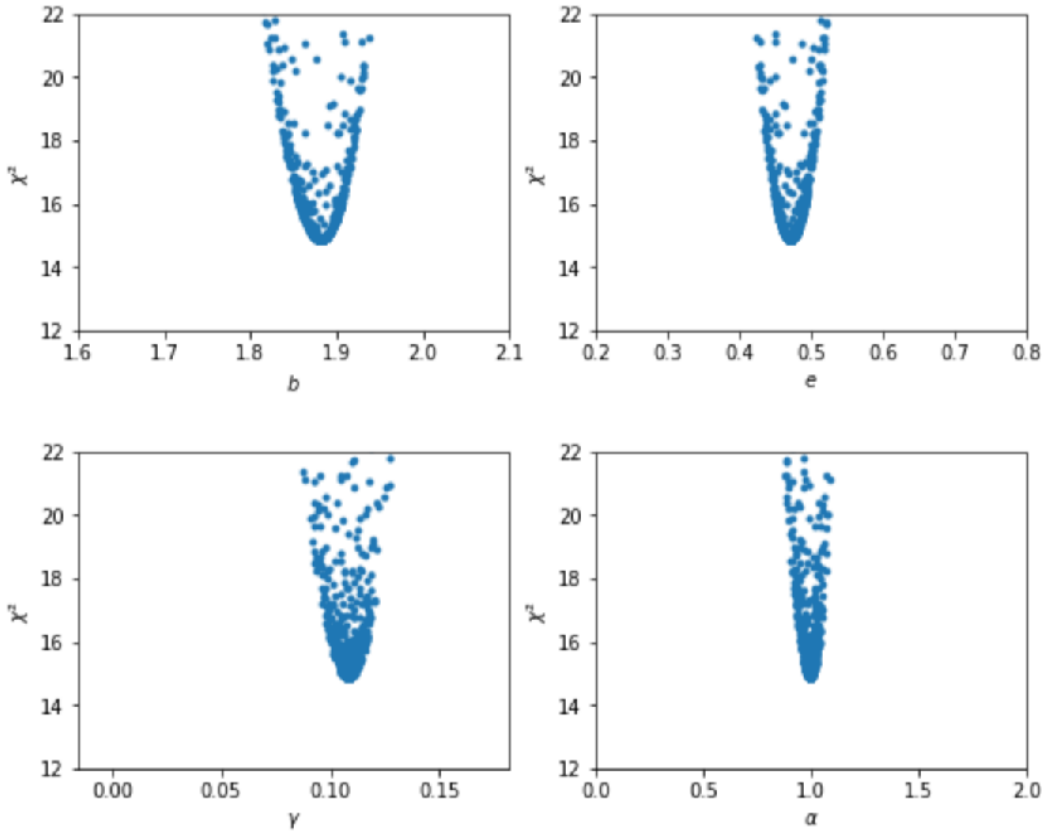

Figure 5.5: Total χ^2 plots for the fit **4** of the cusp configuration, evaluated in the source plane, with respect to the parameters b', e, γ, and α.

Nonetheless, all the parameters were not free for the randomization in the source plane of the first four fits and one realizes that when all the parameters, including α, are liberated in the randomization of the fit **5**, it results in a mass model which is very different (Table 5.1). The χ^2 of the fit **5** is much better than the one of the fit **4** (Table 5.2) because the contribution of the time delays has dropped significantly. Moreover, it can be seen on Figure 5.6 that the fitted parameters seem to correspond to a minimum of χ^2, but it is less pronounced. Of course, this statement is due to the fact that all parameters are free to vary and therefore leading to more possibilities of degenerated mass models. Furthermore, if one looks at the Figure 5.7, one notices that the inner critical line is ridiculously small and above all, one notices that the outer caustic is extremely large ($\approx$ 500 arcsec radius). This observation leads one to think that the mass model relating to the fit **5** is non-physical.

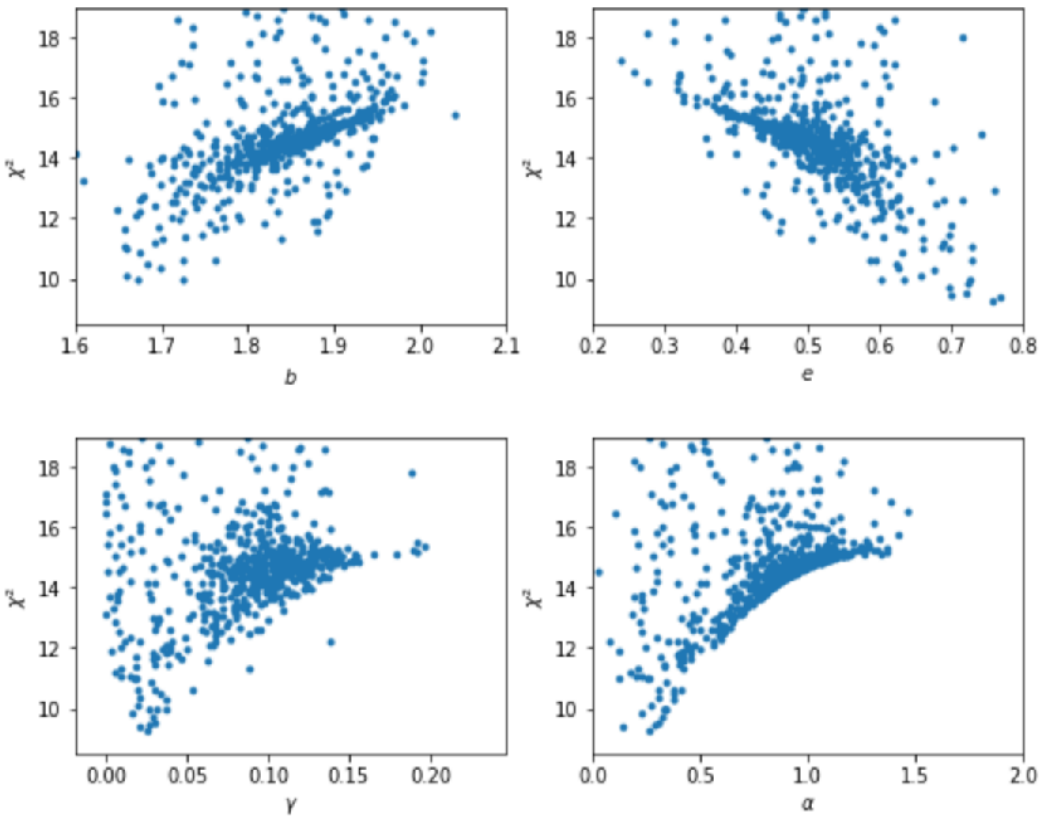

Figure 5.6: Total χ^2 plots for the fit **5** of the cusp configuration, evaluated in the source plane, with respect to the parameters b', e, γ, and α.

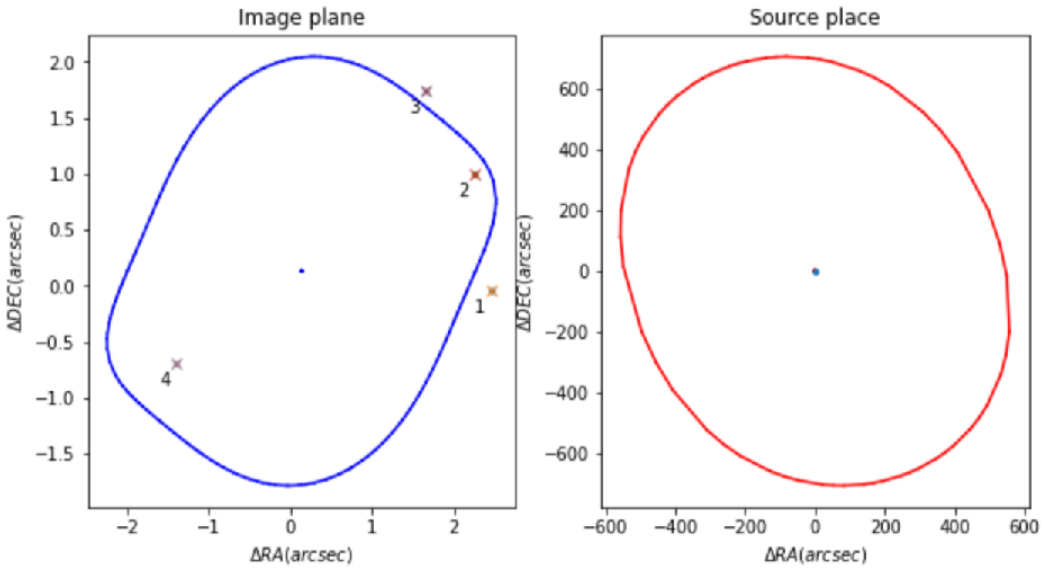

Figure 5.7: Plot of the critical lines and caustics constructed on the basis of the model relating to the fit **5**. The four images are represented by a cross in the image plane and the source is denoted by a dot in the source plane.

In addition, it is interesting to compare the best fitted model directly with the mock lens that has been used to build the lensing system. To that end, the κ map (Figure 5.4) is fitted with "elliptical isophotes" (in this case they correspond to elliptical isodensities) thanks to Photutils, an Astropy package for detection and photometry of astronomical sources [3]. In other words, an algorithm implemented in Photutils allows one to fit ellipses to the pixels intensities of Figure 5.4 in order to describe the azimuthally averaged radial distribution of the mock lens.

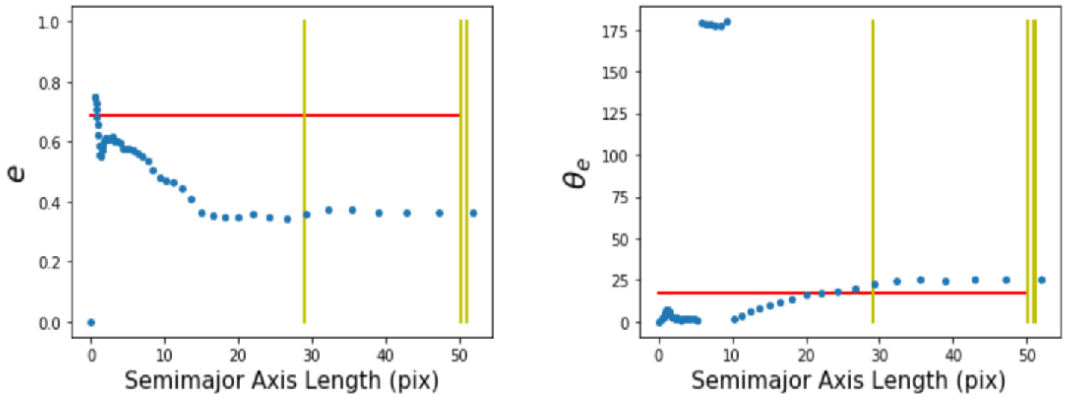

Figure 5.8: Comparison of the ellipses fitted to the κ map of the mock lens with the model parameters relating to the fit **5**. The ellipticity (e) and the position angle of the ellipticity (θ_e) of the different ellipses are plotted with respect to the semimajor axis length measured in pixels (1 pixel = 0.05 arcsec). The definition of the ellipticity is the same as the one previously introduced, but the position angle is measured from the East axis, counter clockwise. The red horizontal lines represent the parameter relating to the fitted mass model. The yellow vertical lines stand for the positions of the four images. Note that for the region below $\approx$ 10 pixels, the e and θ_e are not robustly retrieved by the fitting methods, such that the blue symbols in that range must be ignored.

The comparison of the fitted ellipses with respect to the model parameters is realized on Figure 5.8. One can see that the ellipticity (e) is not well retrieved at all. Nevertheless, the position angle of the ellipticity (θ_e) seems to be more or less well fitted between the two most distant images.
Moreover, the comparison of the κ profiles of the mock lens and the model in logarithmic scale are showed in Figure 5.9. The κ profile of the model can be generated in the same way as for the mock lens, by Photutils and using the κ map created with *lensmodel* on the basis of the fitted parameters of the model. It is clear that these two profiles are very different in terms of values of κ as well as in terms of shape, the profile of the mock lens is evidently non-linear in logarithmic scale and it seems to be an evidence for a core radius in the central region.

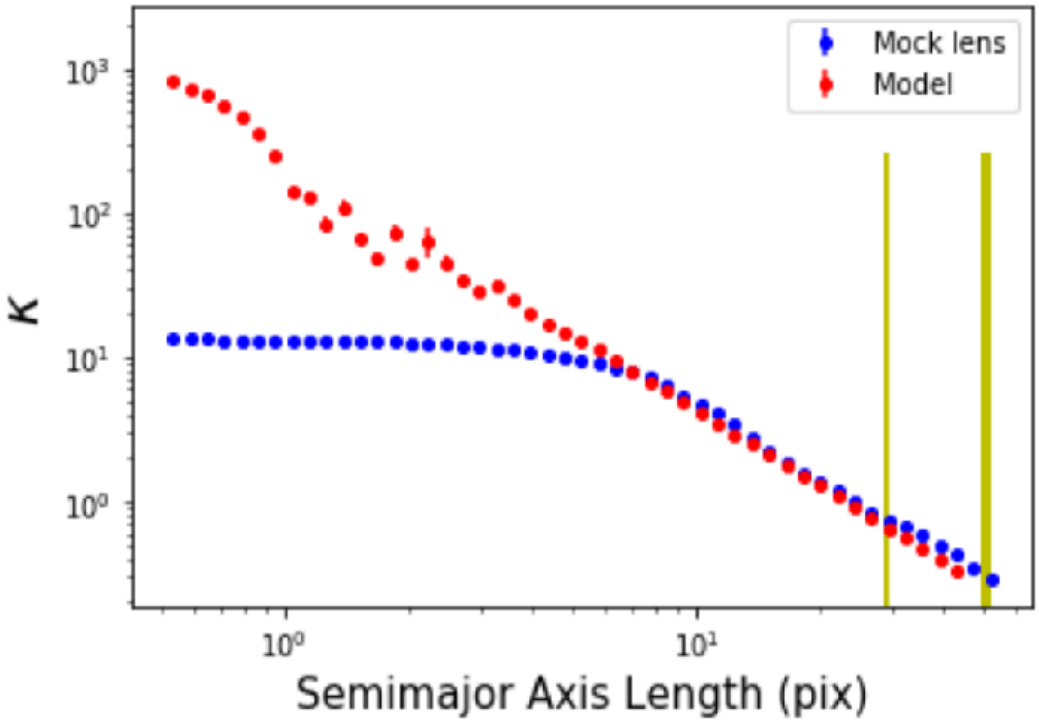

Figure 5.9: Comparison of the κ profile of the mock lens (blue) with the kappa profile of the model (red), in logarithmic scale. The yellow vertical lines stand for the positions of the four images. The well-pronounced non-linearity of the κ profile of the model at low semimajor axis may be due to the issues with the fitting method below 10 pixels.

Furthermore, it would be interesting to evaluate the slope of the κ profile of the mock lens between the two most distant images in order to verify if the fitted power-law index α of the best model (fit **5**) gives the same slope. To that end, one performs a linear regression of this κ profile between the two most distant images and it results in a slope equal to -1.427. The analytic slope of κ in log scale, derived from the relation (3.2), is $\alpha - 2$. The fitted value of α is 0.241, hence resulting in an analytic slope of -1.759. Therefore, it seems that the slope of the model is not well fitted, this could be due to the fact that , despite the good χ^2, the fitted model does not look very physical.

In addition, it would be relevant to compare the κ map of the mock lens with the κ map generated on the basis of the fitted parameters of the model. In Figure 5.10, the normalized residuals between the κ maps of the mock lens and the model have been plotted. One can see that the residuals are really significant and notably on areas far from the center. It shows that the mass distribution of the model drops to zero more quickly than the one of mock lens, because its slope is greater than the slope of the mock, as it

can be seen in Figure 5.9.
Finally, one can also see on the center of Figure 5.10 that the κ of the model is very large compared to the mock lens (the dark blue central region), reflecting the fact that, perhaps, a core radius should be considered in the mass model because κ is by far too important in the vicinity of the center.
Therefore one can infer that, for the cusp configuration, the analytical fitted mass distribution does not seem to reproduce well the mass distribution of the mock lens.

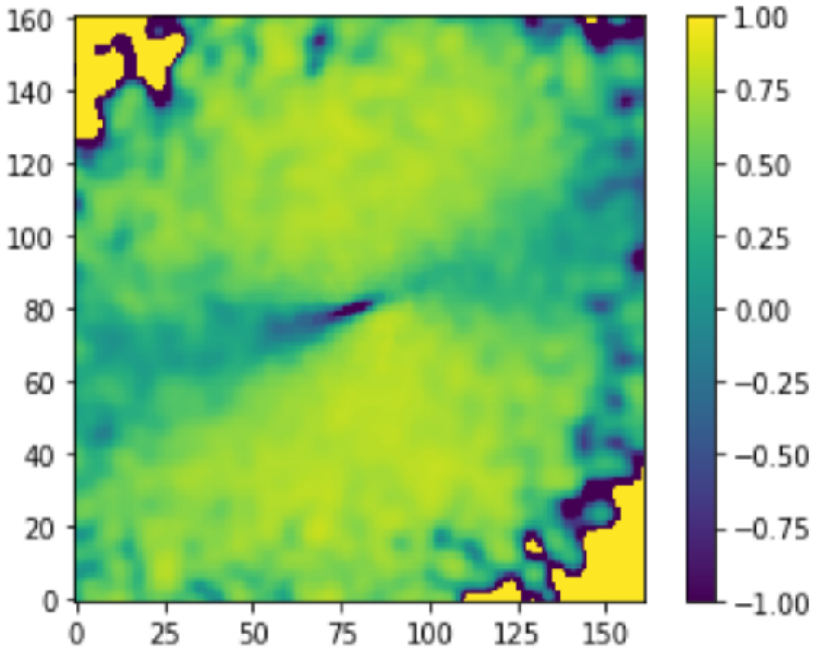

Figure 5.10: Normalized residuals between the κ map of the mock lens and the κ map generated on the basis of the fitted parameters. The residuals are normalized by the mock map and 1 pixel=0.05 arcsec.

5.3 Fold configuration

The fitted parameters for the fold configuration with respect to the different fitting steps are presented in Table 5.3. The situation is almost the same as for the cusp, the fits **1** to **4** do not seem to converge towards the best fit (fit **5**). Indeed, the fitted parameters of the latter are rather different from the other fits. Moreover, it can be seen on Table 5.4 that the total χ^2 relating to the fit **5** is very good (the reduced χ^2 is very close to one)

contrary to the other fits. The randomization of the fit **5** in the source plane is shown in Figure 5.11, for which all the parameters except *s'* have been relaxed. One can see that the fitted parameters correspond well to a global minimum, even if the fitted value of *b'* is far away from the minimum.

	b'	x	y	e	θ_e	γ	θ_γ	s'	α
1	1.580	-0.163	-0.210	0.753	-65.261	0.220	22.903	(0.0)	(1.0)
2	1.860	-0.013	-0.061	0.532	-64.841	0.115	21.973	(0.0)	(1.0)
3	1.860	-0.013	-0.061	0.531	-64.841	0.115	21.973	(0.0)	1.0
4	1.617	-0.189	-0.219	0.742	-65.047	0.240	23.415	(0.0)	1.069
5	1.938	0.174	0.051	0.660	-64.931	0.022	-62.520	(0.0)	0.117

Table 5.3: Comparison of the fitted lens parameters for the fold configuration. The parameters into brackets are fixed and the values are rounded to the third decimal.

	tot	**pos**	**flux**	**tdel**	**gal**	**dof**
1	1.803682e+01	9.255589e-02	1.659088e+01	2.273873e-01	1.125990e+00	7
2	1.258595e+01	3.380437e-02	1.249008e+01	0.000000e+00	6.205668e-02	4
3	1.258506e+01	3.157930e-02	1.249142e+01	0.000000e+00	6.205668e-02	3
4	1.767781e+01	1.610923e-01	1.530545e+01	8.674697e-01	1.343792e+00	6
5	7.809084e+00	3.199900e-01	6.385724e+00	5.762974e-01	5.270733e-01	6

Table 5.4: Comparison of the χ^2 for the fold configuration, with the degrees of freedom in the last column.

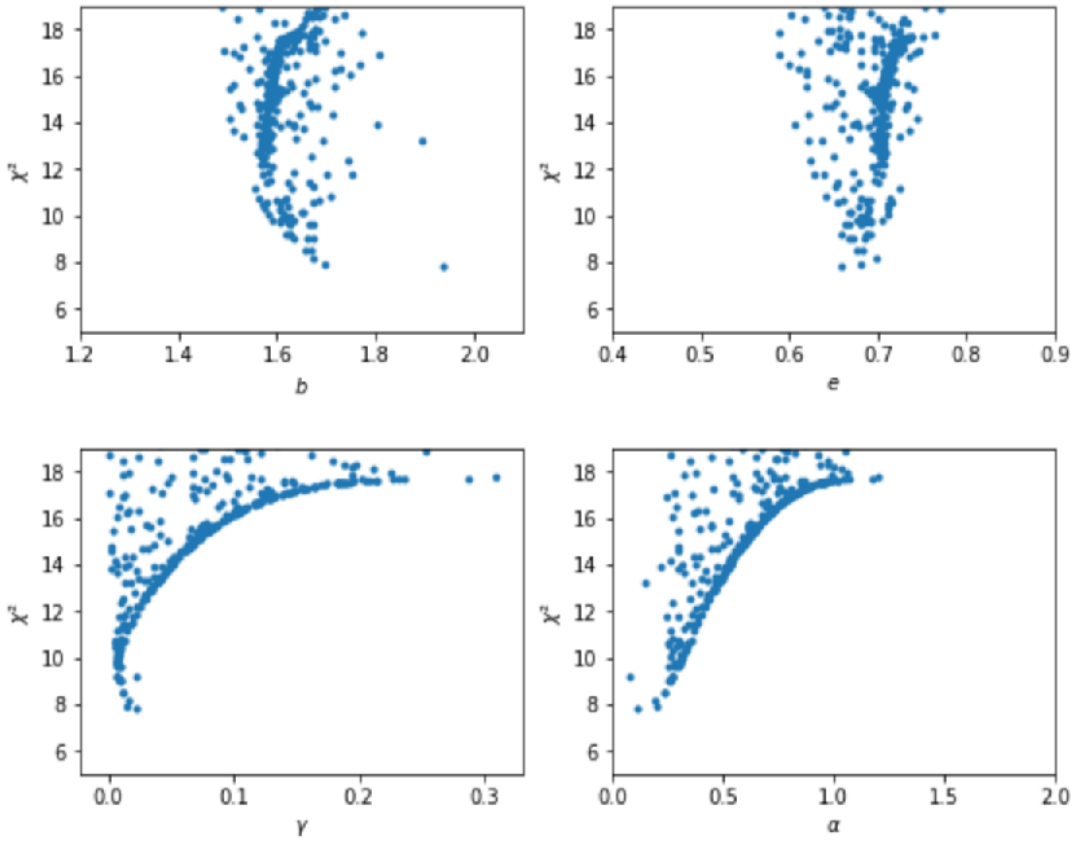

Figure 5.11: Total χ^2 plots for the fit **5** of the fold configuration, evaluated in the source plane, with respect to the parameters *b'*, *e*, γ, and α.

The fitted model seems to be quite robust since the fitted parameters converged towards a global minimum. However, if one takes a look at the Figure 5.12, one can note the same issue as for the cusp configuration, the inner critical line is very small and the outer caustic is way too large. Hence, it would mean that the fitted model is once again non-physical.

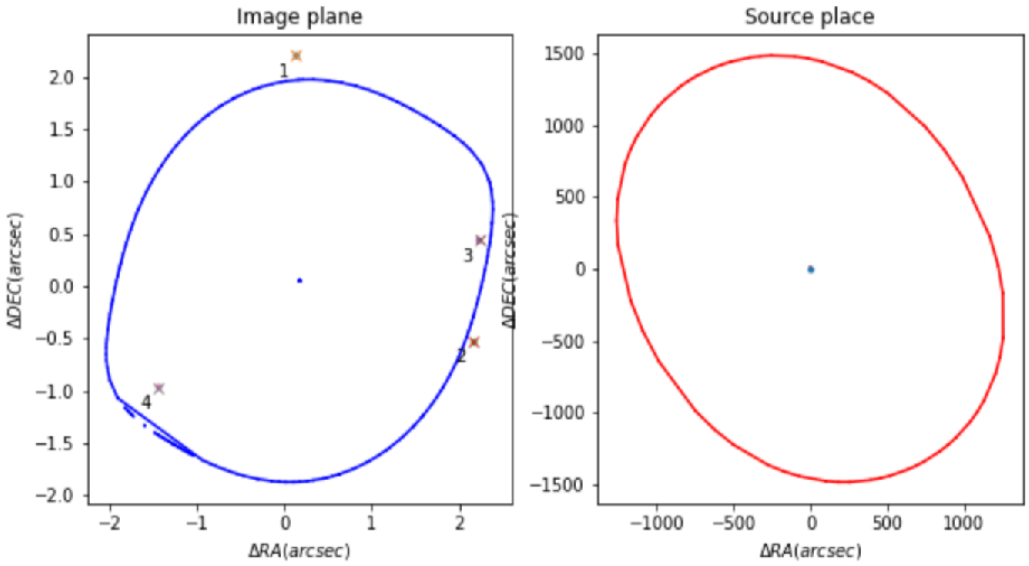

Figure 5.12: Plot of the critical lines and caustics constructed on the basis of the model relating to the fit **5**. The four images are represented by a cross in the image plane and the source is denoted by a dot in the source plane.

The comparison of the best-fitted model parameters with the mock lens is realized on Figure 5.13. One notices that the ellipticity e of the model is again much larger than the ellipticity of the elliptical isophotes of the mock lens. By contrast, the position angle θ_e seems very well retrieved between the two most distant images.

Furthermore, the comparison between the κ profiles of the mock lens and the model is shown on Figure 5.14. It can be seen that the two profiles are once again very different in terms of values of κ and in terms of shape. If one evaluates the slope of the mock lens profile between the two most distant images, the value of -1.505 is obtained, while the slope derived from the model is equal to -1.883 ($\alpha - 2$). Hence, the slope of the model appears not well fitted, it is again probably due to the fact that the fitted model does not look very physical.

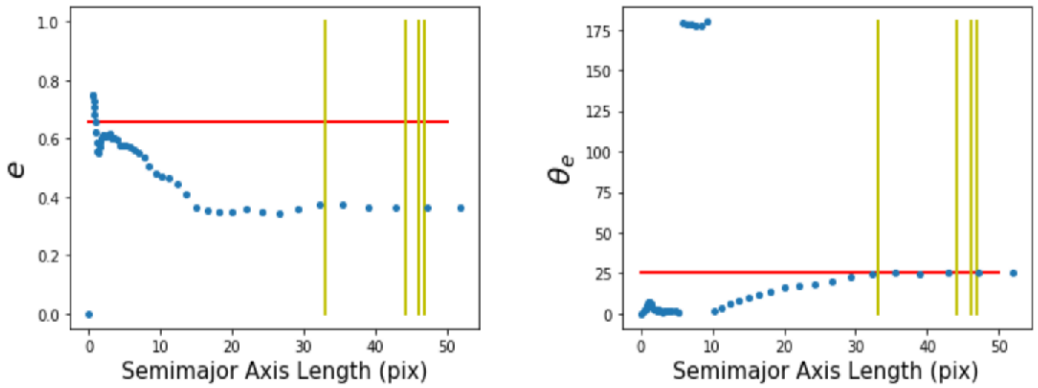

Figure 5.13: Comparison of the ellipses fitted to the κ map of the mock lens with the model parameters relating to the fit **5**. The ellipticity (e) and the position angle of the ellipticity (θ_e) of the different ellipses are plotted with respect to the semimajor axis length measured in pixels (1 pixel = 0.05 arcsec). The definition of the ellipticity is the same as the one previously introduced, but the position angle is measured from the East axis, counter clockwise. The red horizontal lines represent the parameter relating to the fitted mass model. The yellow vertical lines stand for the positions of the four images. Note that for the region below $\approx$ 10 pixels, the e and θ_e are not robustly retrieved by the fitting methods, such that the blue symbols in that range must be ignored.

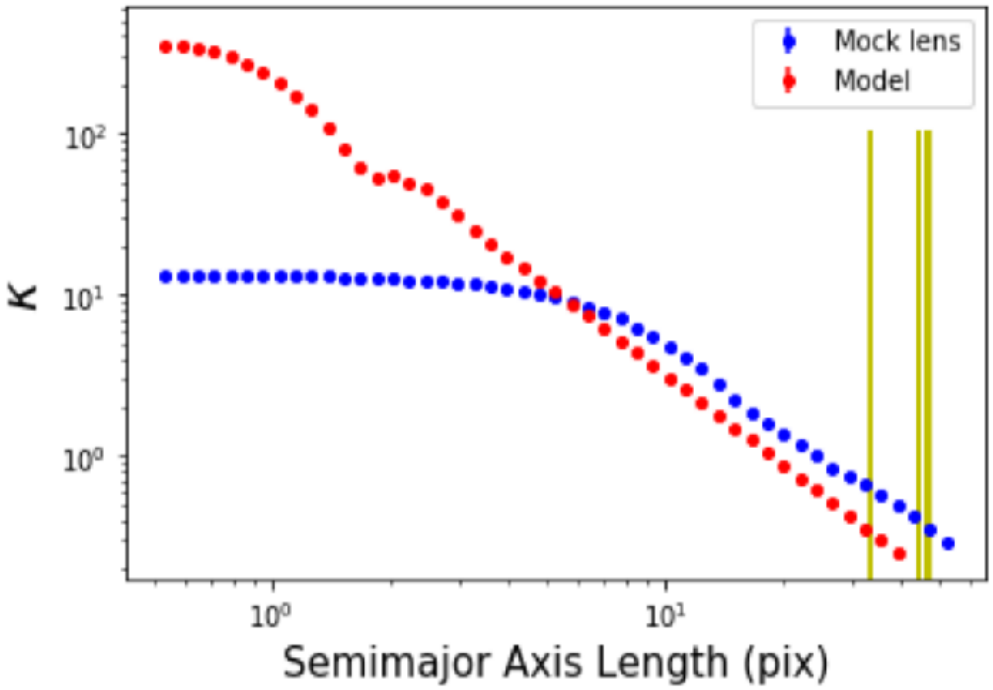

Figure 5.14: Comparison of the κ profile of the mock lens (blue) with the kappa profile of the model (red), in logarithmic scale. The yellow vertical lines stand for the positions of the four images. The well-pronounced non-linearity of the κ profile of the model at low semimajor axis may be due to the issues with the fitting method below 10 pixels.

Finally, on Figure 5.15, the κ maps of the mock lens and the fitted model are compared. The normalized residuals are very considerable all over the field in the same way as for the cusp model. Once again, this could explain why the model tends to derive an ellipticity much larger than observed and it shows that the mass distribution of the mock lens is much more extended than the one of the model. The residuals in the center are also highly negative because the κ of the model is significantly greater than the κ of the mock lens, once more reflecting the fact that, maybe, a core radius should be considered. Therefore, the fitted analytical mass distribution of the fold configuration does not seem to reproduce well the mass distribution of the mock lens.

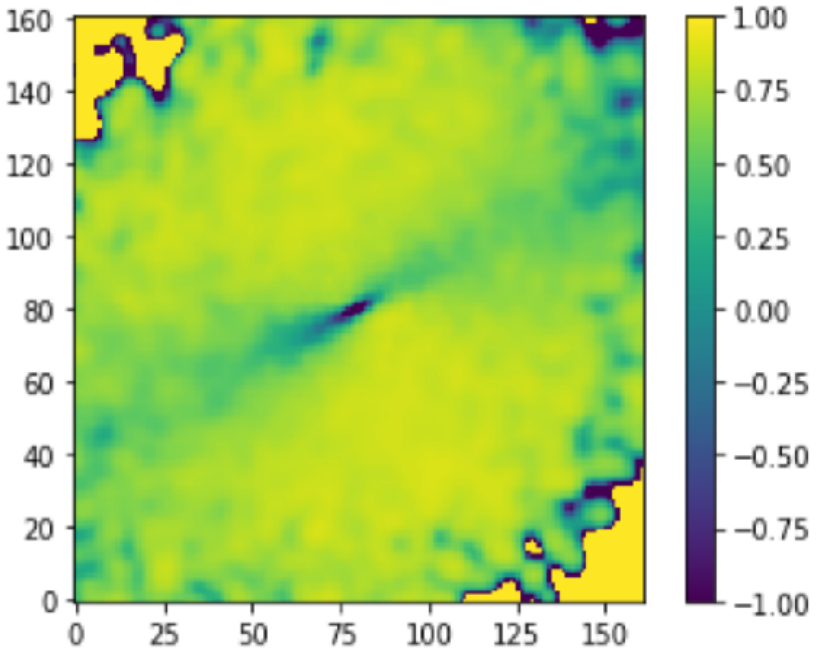

Figure 5.15: Normalized residuals between the κ map of the mock lens and the κ map generated on the basis of the fitted parameters. The residuals are normalized by the mock map and 1 pixel=0.05 arcsec.

5.4 Cross configuration

The fitted parameters for the cross configuration with respect to the different fitting steps are presented in Table 5.5. The model seems refined through all the fitting steps, however, it can be seen in Table 5.6 that the total χ^2 is rather large, except for the fits for which the time delays are not considered as constraints. Indeed, the relatively high reduced χ^2 (≈ 5) of the last fitting step (fit **5**) comes mainly from the time delays that are not very well retrieved.

Moreover, one can see on Figure 5.16 that the randomization in the source plane of the fit **5** leads to parameters such as *b'* and *e* that corresponds to a global minimum of χ^2. Nonetheless, the fitted shear γ and power law index α do not correspond to an explicit minimum of χ^2 and thus, these parameters are perhaps not properly fitted. Indeed, if one plots γ as a function of α (Figure 5.17), one can see that it seems to be a degeneracy between these two parameters.

	b'	*x*	*y*	*e*	θ_e	γ	θ_γ	*s'*	α
1	1.907	0.105	0.008	0.489	-67.324	0.094	18.875	(0.0)	(1.0)
2	1.965	0.109	0.011	0.393	-68.325	0.067	15.915	(0.0)	(1.0)
3	1.965	0.109	0.011	0.393	-68.323	0.067	15.924	(0.0)	1.0
4	1.964	0.109	0.012	0.396	-68.319	0.068	15.954	(0.0)	0.999
5	1.914	0.099	0.004	0.509	-67.062	0.154	21.088	(0.0)	1.241

Table 5.5: Comparison of the fitted lens parameters for the cross configuration. The parameters into brackets are fixed and the values are rounded to the third decimal.

	tot	**pos**	**flux**	**tdel**	**gal**	**dof**
1	3.064762e+01	1.388899e-01	1.780465e+00	2.854966e+01	1.786114e-01	7
2	1.255168e+00	3.792283e-04	1.063162e+00	0.000000e+00	1.916264e-01	4
3	1.255173e+00	4.065526e-04	1.063199e+00	0.000000e+00	1.915678e-01	3
4	3.150872e+01	1.641409e-01	1.071930e+00	3.007938e+01	1.932700e-01	6
5	3.035146e+01	1.467685e-01	1.476524e+00	2.857064e+01	1.575284e-01	6

Table 5.6: Comparison of the χ^2 for the cross configuration, with the degrees of freedom in the last column.

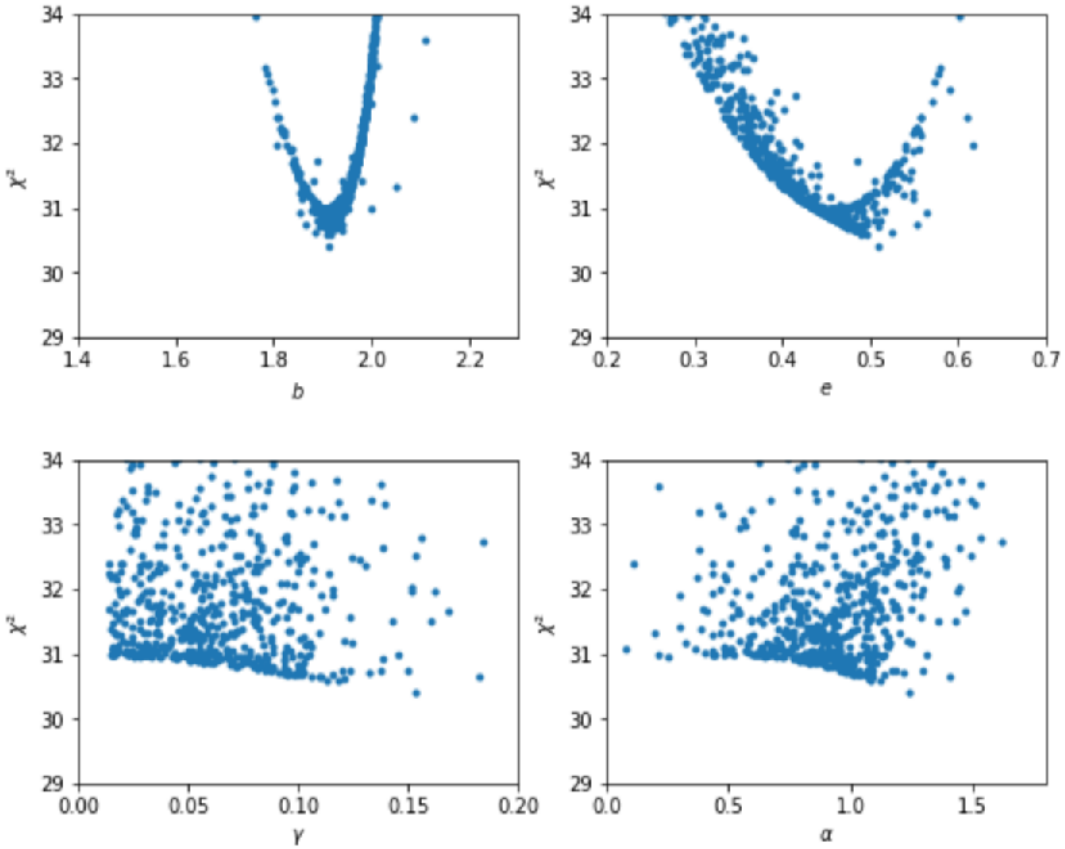

Figure 5.16: Total χ^2 plots for the fit **5** of the cross configuration, evaluated in the source plane, with respect to the parameters b', e, γ, and α.

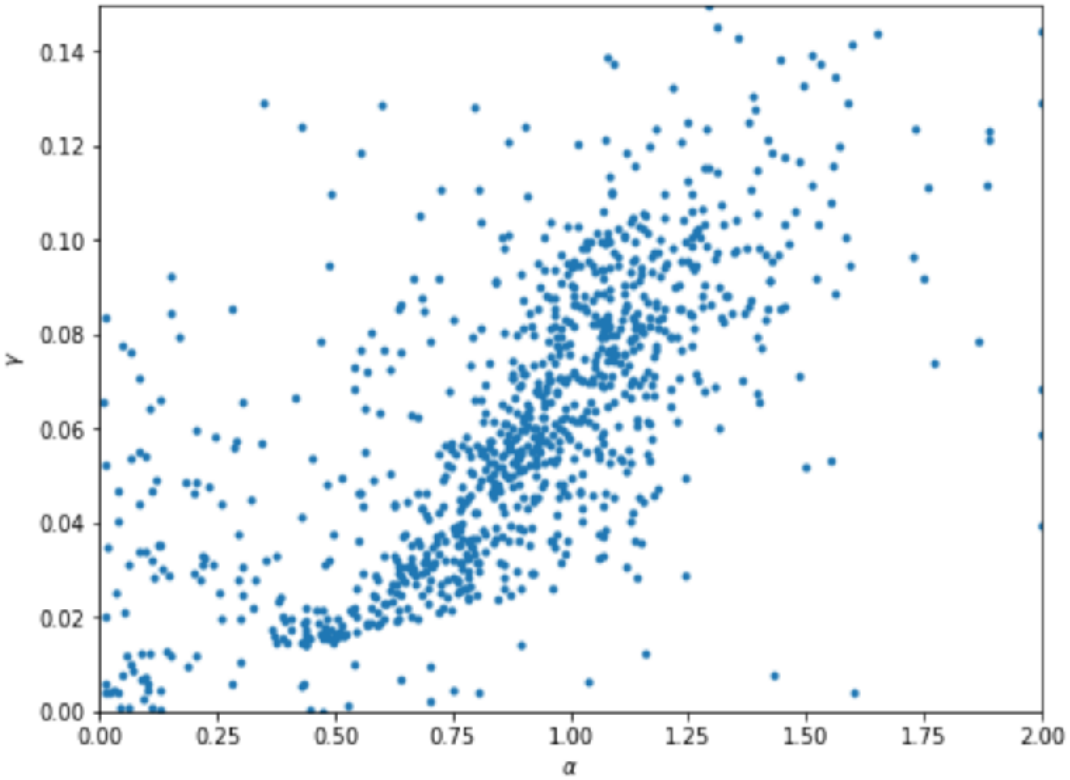

Figure 5.17: Plot of the external shear γ with respect to the power law index α, illustrating the degeneracy between these two parameters.

The critical lines and the caustics are plotted in Figure 5.18 and contrary to the previous configurations, the model seems physical, one can distinguish the two critical lines and the two caustics as well as the images positions and the source position.

The comparison between the model parameters and the fitted ellipses of the mock lens is achieved on Figure 5.19. The ellipticity e of the model is still too large compared to the mock lens, but the fitted position angle θ_e matches well with the position angle of the mock lens.

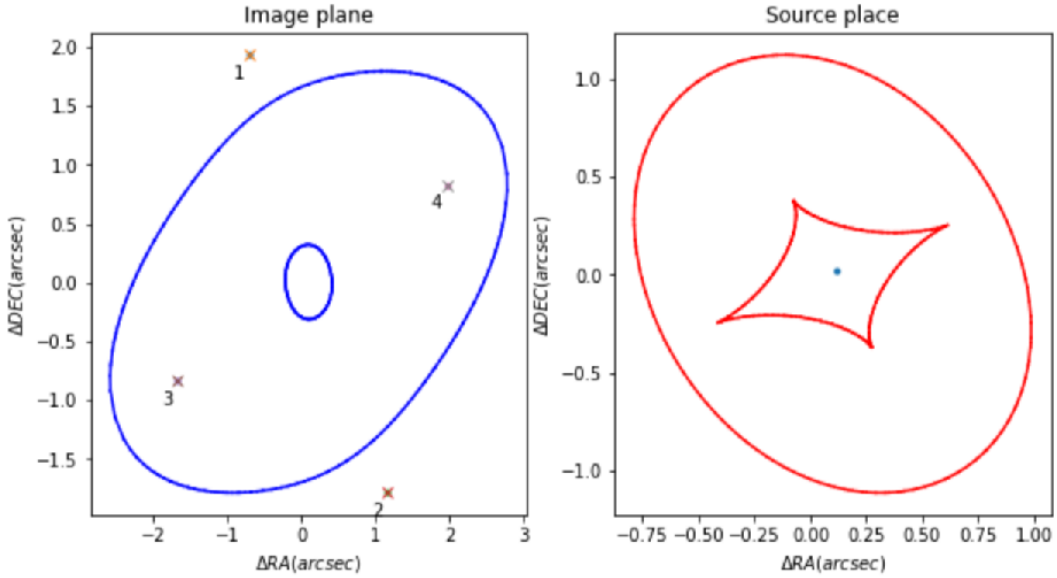

Figure 5.18: Plot of the critical lines and caustics constructed on the basis of the model relating to the fit **5**. The four images are represented by a cross in the image plane and the source is denoted by a dot in the source plane.

Furthermore, the comparison between the κ profiles of the mock lens and the model is presented on Figure 5.20. One may note that, the profiles are again different, but this time, the slopes of the density profiles are clearly distinct. Moreover, at low semimajor axis, the values of κ of the model are closer to the ones of the mock lens in comparison with the two others lensing configurations.

The slope of the mock lens profile between the two most distant images is equal to -1.420 and the slope $\alpha - 2$ derived from the model is equal to -0.759. These slopes are very different whereas the fitted model seems physical. This statement could be due to the fact that, as one has seen on Figure 5.16, the fitted power law index α does not correspond to a well-pronounced global minimum of χ^2 and is not well retrieved.

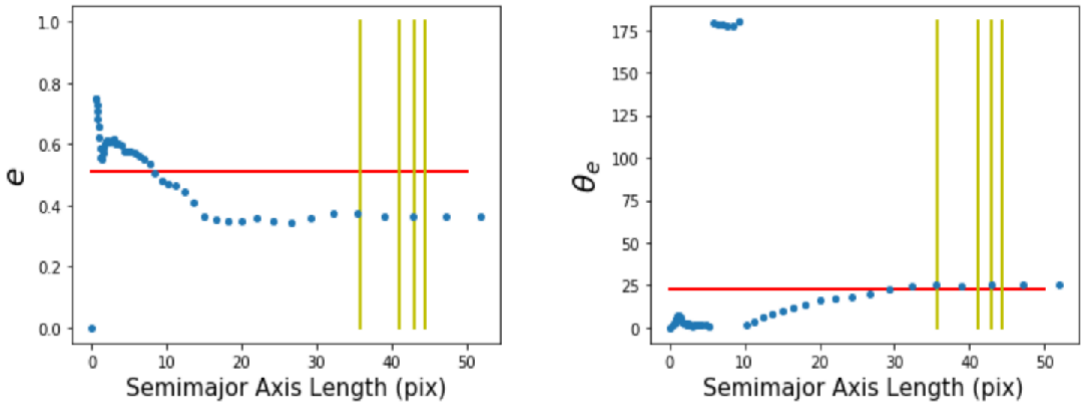

Figure 5.19: Comparison of the ellipses fitted to the κ map of the mock lens with the model parameters relating to the fit **5**. The ellipticity (e) and the position angle of the ellipticity (θ_e) of the different ellipses are plotted with respect to the semimajor axis length measured in pixels (1 pixel = 0.05 arcsec). The definition of the ellipticity is the same as the one previously introduced, but the position angle is measured from the East axis, counter clockwise. The red horizontal lines represent the parameter relating to the fitted mass model. The yellow vertical lines stand for the positions of the four images. Note that for the region below $\approx$ 10 pixels, the e and θ_e are not robustly retrieved by the fitting methods, such that the blue symbols in that range must be ignored.

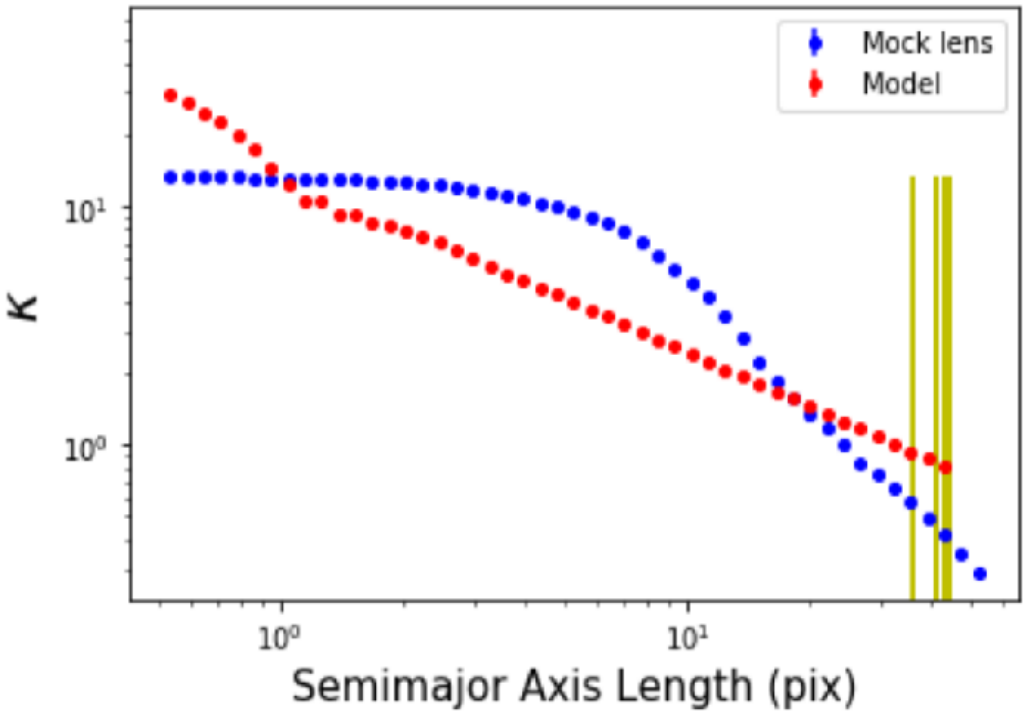

Figure 5.20: Comparison of the κ profile of the mock lens (blue) with the kappa profile of the model (red), in logarithmic scale. The yellow vertical lines stand for the positions of the four images. The well-pronounced non-linearity of the κ profile of the model at low semimajor axis may be due to the issues with the fitting method below 10 pixels.

Finally, the κ maps of the mock lens and the fitted model are compared on Figure 5.21. It can be seen that the normalized residuals are very different from the residuals of the cusp and fold configurations. Indeed, this time the residuals are much less significant especially on the center and it is instead the convergence of the model which is prevailing at large distances (the wide dark blue region). It is easily explainable by the fact that the slope of the model is smaller than the slope of the mock lens, resulting in a convergence that is still high at large distances.

Moreover, the fitted mass model of the cross configuration does not seem to need a core radius, even if one can see a small dark blue dot at the center which indicates that κ of the model is much larger than κ of the mock lens at this specific pixel.

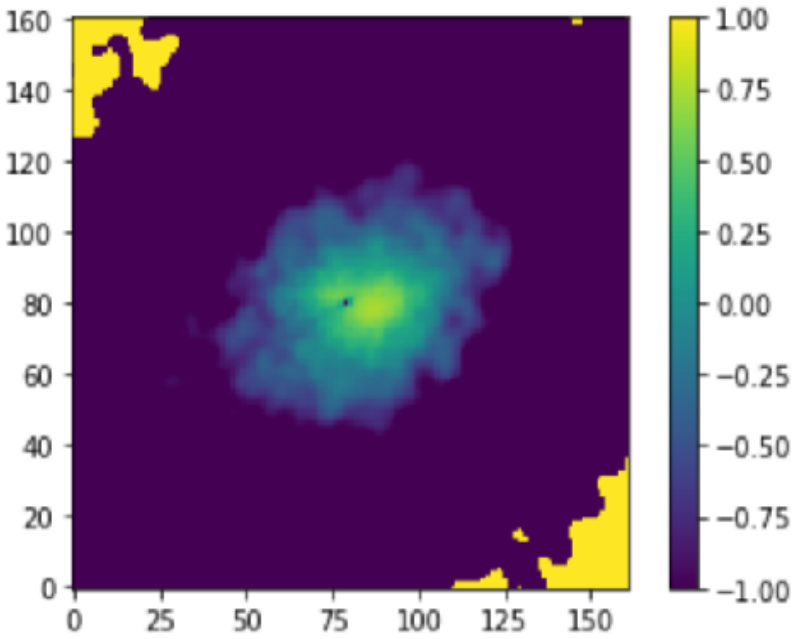

Figure 5.21: Normalized residuals between the κ map of the mock lens and the κ map generated on the basis of the fitted parameters. The residuals are normalized by the mock map and 1 pixel=0.05 arcsec.

5.5 General discussion

The best-fitted model parameters of each configuration discussed in the previous sections are presented in Table 5.7. The fitted mass models relating to the cusp and fold configurations are quite similar regarding their respective reduced χ^2 that are rather equivalent and small, as shown in Table 5.8. However, these χ^2 are not due to the same constraints. Indeed, the χ^2 of the cusp configuration comes from the time delays and it comes from the flux ratios for the fold configuration. On the other hand, the fitted parameters for the cross configuration are relatively different from the other two configurations, the ellipticity e is much smaller and the external shear γ as well as the power law index α are much larger.

	b'	x	y	e	θ_e	γ	θ_γ	s'	α
cusp	1.624	0.136	0.132	0.689	-72.950	0.080	-16.008	0.0	0.241
fold	1.938	0.174	0.051	0.660	-64.93131	0.022	-62.520	0.0	0.117
cross	1.914	0.099	0.004	0.509	-67.062	0.154	21.088	0.0	1.241

Table 5.7: Comparison of the best fitted lens models for the different lens configurations.

	tot	**pos**	**flux**	**tdel**	**gal**	**dof**
cusp	5.444313e+00	9.447160e-03	4.131328e-01	4.449114e+00	5.726191e-01	6
fold	7.809084e+00	3.199900e-01	6.385724e+00	5.762974e-01	5.270733e-01	6
cross	3.035146e+01	1.467685e-01	1.476524e+00	2.857064e+01	1.575284e-01	6

Table 5.8: Comparison of the χ^2 relating to the best fitted model of each configuration, with the degrees of freedom in the last column.

Moreover, one can notice that, as for the cusp configuration, the χ^2 of the cross configuration comes mainly from the time delays. It is surprising because, if one looks at the Table 5.9, one notes that the Hubble constant H_0 is better retrieved for the cross configuration, whereas the inference of H_0 is directly related to the time delays as mentioned in the theory chapter (remember that one proceeds to the modelling of a lens galaxy created considering $H_0 = 67.7 kms^{-1}Mpc^{-1}$). The latter observation is even more surprising because the value of H_0 is also related to the surface mass density between the images, i.e. to the slope of the density profile ($\alpha - 2$), which is very small and which seems not correctly retrieved [11]. In fact, H_0 depends on the observables and the slope but also on the external shear [26], which is substantially higher in the cross configuration than in the cusp or fold configurations. These two aspects might in fact compensate each other and explaining why the Hubble constant is better retrieved in comparison with the two other configurations. The high χ^2 relating to the time delays of the cross configuration could

be simply justified by the fact that the time delay distribution is very sensitive to the slope for power-law profiles, steeper inner slopes tend to produce larger time delays [16]. The same statement can be done, to a less extent, for the model of the cusp configuration, but it is not too critical since its reduced χ^2 is close to 1.

Furthermore, the relatively high contribution of the flux ratios to the χ^2 for the fold configuration could be explained by the fact that one considers point-like images and, as shown on Figure 5.2, two images are almost merging, reflecting the fact that the source is near the fold caustic. Hence, the merging images cannot be considered as point-like images, but rather as extended images in order to properly fit the fluxes ratios.

One may add that it is unexpected to obtain such a large external shear γ for the model of the cross configuration. Indeed, the mock lens generated by hydrodynamical simulations is supposed to be isolated and not undergo the influence of surrounding matter. This leads one to think that the mass model relating to the cross configuration involves parameters which do not correspond well to their true values [6]. In fact, as one has seen on Figure 5.17, it seems to be a degeneracy between γ and α and, as already mentioned, the fitted parameters α and γ do not correspond to a well-pronounced minimum of χ^2 (Figure 5.16. Hence, the fitted mass model of the cross configuration is most probably degenerated. This degeneracy implies that a low γ yields a χ^2 that is not much larger than the one reported and is therefore not excluded by the data.

	θ_E	H_0
cusp	2.013	71.980
fold	2.037	63.674
cross	2.070	68.740

Table 5.9: Comparison of the best fitted Einstein radius and Hubble constant for each configuration.

Finally, as shown by Chae et al. [4], the shape and the number of critical lines and caustics are directly related to the ellipticity, the slope and the core radius of the mass model. The latter statement could explain why the critical lines and the caustics of the mass models relating to the cusp and fold configurations (Figures 5.7 and 5.12) are not well plotted. Indeed, one has seen that the ellipticity of these two models is way too large, that the fitted slopes of the two models do not correspond to the slope of the mock

lens between the two most distant images and, moreover, one did not consider a core radius. Hence, all these factors taken together could explain why the models of the cusp and fold configurations seem to be non-physical.

Chapter 6

Conclusion

In Chapter 4, three fake lenses have been created with an analytical softened power-law model and they have been modeled with the same mass model. The modelling consisted in reproducing the astrometry of the point-source, the lens galaxy position, as well as the time delays between the images. One has seen that a softened power-law mass model retrieves relatively well the parameters of a lens galaxy generated using the same model family. Indeed, the small differences of the fitted model parameters with respect to the parameters used to create the lens system are mainly due to the Gaussian noise added on the data.

However, the modelling of an hydrodynamically simulated lens galaxy performed in Chapter 5 revealed that an analytical lens model such as the softened power-law model experiences difficulties to retrieve the properties of a non-analytic lens. Indeed, the inferred ellipticity of the fitted lens models was clearly too large with respect to the one of the mock lens, expect for the cross configuration for which the ellipticity was better recovered. More importantly, the radial profile of the analytical mass model employed does not match well with the mass distribution of the mock lens. The slopes of the density profiles of the fitted mass models, relating to the three lensing configurations and evaluated between the two most distant images, are quite different from the slope of the mock lens density profile evaluated in the same region. Therefore, it would appear that a rather simple analytical mass model, commonly used in the modelling of strong lensing systems, does not properly constrain a realistic lens model, even if this kind of unsophisticated model is sufficient to retrieve rather correctly the images positions and flux ratios.

One has mentioned that the issues encountered may be due to the fact that one did not consider a core radius in the mass distribution of the model, while the hydrodynamical mass distribitution shows a proeminent core in the central region. Hence, I performed

some additional fits, this time allowing the core radius to vary. These fits returned mass model parameters that were sensibly the same as the ones of the previous fits, with a very small core radius. Thus, the potential solution related to the inclusion of a core radius does not seem to be valid.

Nonetheless, another possible solution involving a better modelling technique might exist. In fact, the constraints could be too poor to adequately constrain the lens mass distribution. It is therefore necessary to evaluate if the same results stand when more advanced lens modelling is performed. Indeed, one considered only point-like images corresponding to the images of the source quasar. In reality, images of the host galaxy are also seen such that extended lensed images are observed. Therefore, it has to be seen if considering extended images as constraints in the modelling of hydrodynamical simulated lenses could lead to much more convenient inferred lens properties. Extended images are effectively used for cosmography, but such a lens modelling is much more computationally expensive and is beyond the scope of this master thesis.

Bibliography

[1] The EAGLE project. http://icc.dur.ac.uk/Eagle/index.php. Accessed: 2020-08-14.

[2] BIRRER, S., AND AMARA, A. lenstronomy: Multi-purpose gravitational lens modelling software package. *Physics of the Dark Universe 22* (2018), 189–201.

[3] BRADLEY, L., SIPŐCZ, B., ROBITAILLE, T., TOLLERUD, E., VINÍCIUS, Z., DEIL, C., BARBARY, K., GÜNTHER, H. M., CARA, M., BUSKO, I., CONSEIL, S., DROETTBOOM, M., BOSTROEM, A., BRAY, E. M., BRATHOLM, L. A., WILSON, T., CRAIG, M., BARENTSEN, G., PASCUAL, S., DONATH, A., GRECO, J., PERREN, G., LIM, P. L., AND KERZENDORF, W. astropy/photutils: v0.6, Jan. 2019.

[4] CHAE, K.-H., KHERSONSKY, V. K., AND TURNSHEK, D. A. Gravitational lensing by power-law mass distributions: A fast and exact series approach. *The Astrophysical Journal 506*, 1 (1998), 80.

[5] GAVAZZI, R., TREU, T., RHODES, J. D., KOOPMANS, L. V., BOLTON, A. S., BURLES, S., MASSEY, R. J., AND MOUSTAKAS, L. A. The sloan lens acs survey. iv. the mass density profile of early-type galaxies out to 100 effective radii. *The Astrophysical Journal 667*, 1 (2007), 176.

[6] GOMER, M. R., AND WILLIAMS, L. L. Galaxy-lens determination of *h_0*: constraining density slope in the context of the mass sheet degeneracy. *arXiv preprint arXiv:1907.08638* (2019).

[7] HOGG, D. W. Distance measures in cosmology. *arXiv preprint astro-ph/9905116* (1999).

[8] KEETON, C. gravlens 1.06 software for gravitational lensing, 2004.

[9] KEETON, C. R. A catalog of mass models for gravitational lensing. *arXiv preprint astro-ph/0102341* (2001).

[10] KEETON, C. R. Computational methods for gravitational lensing. *arXiv preprint astro-ph/0102340* (2001).

[11] KOCHANEK, C. What do gravitational lens time delays measure? *The Astrophysical Journal 578*, 1 (2002), 25.

[12] KOOPMANS, L. V., TREU, T., BOLTON, A. S., BURLES, S., AND MOUSTAKAS, L. A. The sloan lens acs survey. iii. the structure and formation of early-type galaxies and their evolution since z 1. *The Astrophysical Journal 649*, 2 (2006), 599.

[13] MAGAIN, P. Lecture notes of "Extragalactic astrophysics", Université de Liège. 2019.

[14] MUKHERJEE, S., KOOPMANS, L. V. E., METCALF, R. B., TESSORE, N., TORTORA, C., SCHALLER, M., SCHAYE, J., CRAIN, R. A., VERNARDOS, G., BELLAGAMBA, F., AND THEUNS, T. SEAGLE - I. A pipeline for simulating and modelling strong lenses from cosmological hydrodynamic simulations. *479*, 3 (Sept. 2018), 4108–4125.

[15] NARAYAN, R., AND BARTELMANN, M. Lectures on gravitational lensing. *arXiv preprint astro-ph/9606001* (1996).

[16] OGURI, M., TARUYA, A., SUTO, Y., AND TURNER, E. L. Strong gravitational lensing time delay statistics and the density profile of dark halos. *The Astrophysical Journal 568*, 2 (2002), 488.

[17] PRESS, W. H., TEUKOLSKY, S. A., VETTERLING, W. T., AND FLANNERY, B. P. *Numerical Recipes in C, The Art of Scientific Computing, Second Edition*. Cambridge University Press, 1992.

[18] RATNATUNGA, K. U., OSTRANDER, E. J., GRIFFITHS, R. E., AND IM, M. New “einstein cross” gravitational lens candidates in hubble space telescope wfpc2 survey images. *The Astrophysical Journal Letters 453*, 1 (1995), L5.

[19] REFSDAL, S., AND SURDEJ, J. Gravitational lenses. *Reports on Progress in Physics 57*, 2 (1994), 117.

[20] SCHNEIDER, P. A new formulation of gravitational lens theory, time-delay, and fermat’s principle. *Astronomy and Astrophysics 143* (1985), 413–420.

[21] SCHNEIDER, P., KOCHANEK, C., AND WAMBSGANSS, J. *Gravitational lensing: strong, weak and micro: Saas-Fee advanced course 33*, vol. 33. Springer Science & Business Media, 2006.

[22] SLUSE, D., CHANTRY, V., MAGAIN, P., COURBIN, F., AND MEYLAN, G. Cosmograil: the cosmological monitoring of gravitational lenses-x. modeling based on high-precision astrometry of a sample of 25 lensed quasars: consequences for ellipticity, shear, and astrometric anomalies. *Astronomy & Astrophysics 538* (2012), A99.

[23] TAGORE, A. S., BARNES, D. J., JACKSON, N., KAY, S. T., SCHALLER, M., SCHAYE, J., AND THEUNS, T. Reducing biases on h 0 measurements using strong lensing and galaxy dynamics: results from the eagle simulation. *Monthly Notices of the Royal Astronomical Society 474*, 3 (2018), 3403–3422.

[24] WALLINGTON, S., AND NARAYAN, R. The Influence of core radius on gravitational lensing by elliptical lenses. *Astrophys. J. 403* (1993), 517.

[25] WONG, K. C., SUYU, S. H., CHEN, G. C., RUSU, C. E., MILLON, M., SLUSE, D., BONVIN, V., FASSNACHT, C. D., TAUBENBERGER, S., AUGER, M. W., ET AL. H0licow xiii. a 2.4% measurement of h0 from lensed quasars: 5.3 σ tension between early and late-universe probes. *Monthly Notices of the Royal Astronomical Society* (2019).

[26] WUCKNITZ, O. Degeneracies and scaling relations in general power-law models for gravitational lenses. *Monthly Notices of the Royal Astronomical Society 332*, 4 (2002), 951–961.

[27] XU, D., SLUSE, D., SCHNEIDER, P., SPRINGEL, V., VOGELSBERGER, M., NELSON, D., AND HERNQUIST, L. Lens galaxies in the illustris simulation: power-law models and the bias of the hubble constant from time delays. *Monthly Notices of the Royal Astronomical Society 456*, 1 (2016), 739–755.